3-D shallow-water seismic survey evaluation and design using the focal-beam method a case study offshore Abu Dhabi

Ishiyama, Tomohide; Blacquière, Gerrit

DOI
10.1111/1365-2478.12335

Publication date
2016

Document Version
Accepted author manuscript

Published in
Geophysical Prospecting

Citation (APA)
Ishiyama, T., & Blacquière, G. (2016). 3-D shallow-water seismic survey evaluation and design using the focal-beam method: a case study offshore Abu Dhabi. *Geophysical Prospecting*, *64*(5), 1215-1234. https://doi.org/10.1111/1365-2478.12335

Geophysical Prospecting (201?) **XX,** 000–000

3-D shallow-water seismic survey evaluation and design using the focal-beam method: a case study offshore Abu Dhabi

Tomohide Ishiyama[1,2⋆], Gerrit Blacquière[1],

[1]*Department of Geotechnology, Faculty of Civil Engineering and Geosciences,*

Delft University of Technology, PO Box 5048, 2600 GA Delft, The Netherlands

[2]*Inpex Corporation, 5-3-1 Akasaka, Minato-ku, 107-6332 Tokyo, Japan*

Corresponding author, E-mail: tomohide.ishiyama@inpex.co.jp

Received August 2014, revision accepted ?? 2014

SUMMARY

For 3-D shallow-water seismic surveys offshore Abu Dhabi, imaging the target reflectors requires high resolution. Characterization and monitoring of hydrocarbon reservoirs by seismic amplitude-versus-offset techniques demands high pre-stack amplitude fidelity. In this region, however, it is still not clear how the survey parameters should be chosen to satisfy the required data quality. To answer this question, we applied the focal-beam method to survey evaluation and design. This subsurface-oriented and target-oriented approach enables quantitative analysis of attributes such as the best achievable resolution and pre-stack amplitude fidelity at a fixed grid point in the subsurface for a given acquisition geometry at the surface. This method offers an efficient way to optimize the acquisition geometry for maximum resolution and minimum amplitude-versus-offset imprint. We applied it to several acquisition geometries in order to understand the effects of survey parameters such as the four spatial sampling intervals and apertures of the template geometry. The results led to a good understanding of the relationship between the survey parameters and the resulting data quality, and identification of the survey parameters for reflection imaging and amplitude-versus-offset applications.

Key words: survey design, shallow water, focusing, resolution, AVO, sensing, illumination, Abu Dhabi

INTRODUCTION

Seismic survey parameters should be chosen such that the acquired data have the quality required to achieve the objectives in exploration, appraisal and development of oil and gas fields. Several authors have presented sophisticated approaches to survey evaluation and design in order to obtain a high data quality while mitigating the survey effort. Traditionally, survey design is based on bin attributes such as fold, offset, azimuth sampling in each bin, as well as their distribution across bins. Such aspects are discussed by Cordsen *et al.* (2000); Galbraith (2004); Vermeer (2012). In this approach, the information is obtained from a given acquisition geometry at the surface, but subsurface structures and properties are not taken into account. Therefore, this approach may be valid for a nearly homogeneous subsurface but it is no longer adequate for a complex subsurface. Recently, survey design has started to involve full simulation of a seismic experiment for a given acquisition geometry, full processing of the simulated seismic data to evaluate the resulting image quality, and full inversion of the processed data to evaluate the resulting quality of the estimated reservoir properties. However, these results include the combined effects of the acquisition geometry, processing and inversion and, therefore, obscure the effects purely due to the given acquisition geometry. In addition, this approach is computationally expensive, making it impractical if acquisition geometries need be designed over and over again. A more efficient approach to survey design involves the reconstruction of the angle-dependent reflectivity in one or more subsurface points in the target area. The input data consist ~~in~~of the waves scattered from a single subsurface point for a given acquisition geometry and an assumed subsurface model. After wave-equation-based pre-stack depth migration, the imaging quality of the reconstructed angle-dependent reflectivity in the subsurface point is then used to evaluate the acquisition geometry. This reflectivity is equivalent to the Hessian for angle-dependent least-squares wave-equation-based pre-stack depth migration (e.g. Ren *et al.* 2011), but evaluated for a subsurface point that does not introduce any angle dependence. An example is the focal-beam method, which was initially developed by Berkhout *et al.* (2001) and Volker *et al.* (2001), and further expanded by van Veldhuizen *et al.* (2008) and Wei *et al.*

(2012). This method makes use of the common focus point (CFP) technology (Berkhout 1997a,b), in which the seismic response is decomposed into individual subsurface points, and the migration response is modelled for one or more specific subsurface points and for a given acquisition geometry. Therefore, this method can be applied to survey evaluation and design as a subsurface-oriented and target-oriented approach to obtain certain attributes for one or more subsurface points rather than for the whole subsurface volume.

In a shallow-water environment like the Gulf region in the Middle East, 3-D ocean bottom cable (OBC) and ocean bottom node (OBN) seismic surveys are often acquired under operational constraints such as shallow-water depths and numerous production facilities distributed in a scattered way over the survey area. In these seismic surveys, receivers and sources are independently deployed. Therefore, the survey design is highly flexible, allowing for a variety of acquisition geometries. Ishiyama *et al.* (2010c, 2012) and Nakayama *et al.* (2013) describe the comprehensive properties of and several options for a shallow-water acquisition geometry. The relevant survey parameters are the four spatial sampling intervals and apertures of the template geometry, similar to those of marine and land seismic surveys (Vermeer 2012). The four spatial sampling intervals are defined by the receiver and source intervals, each in two sampling directions that are usually orthogonal. The four spatial sampling apertures consist ~~in~~of the receiver and source apertures, oriented in the same way as the above four spatial coordinates. Proper spatial sampling can be viewed as the ability to properly reconstruct seismic wavefields. Wide apertures, i.e., a large extent of the template geometry, enhances the ability to reconstruct seismic wavefields in terms of spatial continuity. In addition, this is beneficial for fault imaging and fracture characterization in the region (e.g. Ishiyama *et al.* 2010b).

In the region offshore Abu Dhabi, the structures are generally quite gentle. The main reservoirs are in the Upper Jurassic and the Lower Cretaceous successions, which are all carbonate layers. Obtaining good-quality signals from the reflectors is not always easy, especially in the Upper Jurassic formations, due to the very low impedance contrast and the thin layering. Therefore, a high resolution is demanded to image the reflectors. Applying amplitude-versus-offset (AVO) or amplitude-versus-ray parameter (AVP) techniques is still challenging for carbonate reservoirs because of the well-known fact that the pore fluids have a very subtle effect on the AVP response. In addition, the lithologic complexities result in a variety of AVP behaviours. Nevertheless, some successful cases of AVP applications to carbonate reservoirs exist in the region (e.g. Ishiyama *et al.* 2010a). Therefore, a high pre-stack amplitude fidelity should be reached to meet the requirements of AVP applications for seismic reservoir characterization and monitoring. This situation prompts the following questions for ~~the~~the applications of reflection imaging and AVP ~~applications~~.

(i) What is the relationship between the survey parameters and the resulting data quality?

(ii) Which types of survey parameters are essential?

In this paper, we adopted the focal-beam method to try to answer these questions. This subsurface-oriented and target-oriented approach enables quantitative analysis of the achievable resolution and pre-stack amplitude fidelity for one or more grid points in the subsurface and for a given acquisition geometry at the surface. We start with an overview of the focal-beam method, apply it to 3-D shallow-water seismic survey evaluation and design offshore Abu Dhabi, and end with a discussion on the relationship between the survey parameters and the resulting data quality.

FOCAL-BEAM METHOD

First, we discuss the survey parameters and define survey effort. Then, we summarize the focal-beam method. In this method, migration is described as a double-focusing process to 3-D seismic data. The output is presented as the combined result of focal beams: focal detector beam and focal source beam, revealing the migration response by focal functions: the resolution by resolution function and the pre-stack amplitude fidelity by AVP function. We introduce these concepts briefly but ~~orderly~~sequentially one by one. For further theoretical and mathematical details, we refer the reader to the papers by Berkhout *et al.* (2001), Volker *et al.* (2001), van Veldhuizen *et al.* (2008), and Wei *et al.* (2012). ~~we~~We will adopt the mathematical notation of these authors: matrices are bold with upper case; vectors are in italics with a right-arrow symbol $\vec{\cdot}$. In addition, we will sometimes use the word 'detector' for 'receiver'.

Survey parameters and survey effort

As already mentioned, for 3-D shallow-water seismic surveys, the relevant survey parameters are the spatial sampling intervals for receivers, Δx_d and Δy_d, and for sources, Δx_s and Δy_s, as well as their respective apertures, X_d and Y_d for the receivers and X_s and Y_s for the sources in the template geometry. For an orthogonal geometry, the basic subset is a cross-spread gather, where receiver-point and source-point intervals are quite fine (Δx_d and Δy_s for example), whereas receiver-line and source-line intervals are often coarse (Δy_d and Δx_s in this example). Receiver-line and source-line lengths specify the maximum apertures (X_d and Y_s for this basic subset). For an areal geometry, the basic subset is a common-receiver gather, where receivers are arranged on a sparsely spaced spaced grid (Δx_d and Δy_d) while sources are on a densely spaced grid (Δx_s and Δy_s). Source-spread widths (X_s and Y_s) specify the maximum apertures. This is because deployment of receivers usually requires more effort than that of sources in shallow-water seismic surveys. It should be noted that from these survey parameters traditional survey attributes such as bin size, nominal fold, trace density, maximum offset and largest minimum offset can be directly calculated.

Two of the four spatial coordinates, the set $\{\Delta x_b, \Delta y_b, X_b, Y_b\}$, specify the spatial sampling of the basic subset, where the subscript b can be either d or s, independently for each survey parameter but not in arbitrary combinations. Two other coordinates, the set $\{\Delta x_B, \Delta y_B\}$, specify the spatial redundancy of the basic subsets, i.e., the fold, where again the subscript B can be d or s. Their maximum apertures, X_B and Y_B, are usually the same as X_b and Y_b to form the template. For instance, the set $\{\Delta x_d, \Delta y_s, X_d, Y_s\}$ specifies the spatial sampling of a cross-spread gather, i.e., $\{\Delta x_b, \Delta y_b, X_b, Y_b\} = \{\Delta x_d, \Delta y_s, X_d, Y_s\}$, whereas the set $\{\Delta x_s, \Delta y_d\}$ specifies the spatial redundancy of the cross-spread gather, i.e., $\{\Delta x_B, \Delta y_B\} = \{\Delta x_s, \Delta y_d\}$. For another example, the set $\{\Delta x_s, \Delta y_s, X_s, Y_s\}$ specifies the spatial sampling of a common-receiver gather, whereas the set $\{\Delta x_d, \Delta y_d\}$ specifies the spatial redundancy of the common-receiver gather, i.e., $\{\Delta x_b, \Delta y_b, X_b, Y_b, \Delta x_B, \Delta y_B\} = \{\Delta x_s, \Delta y_s, X_s, Y_s, \Delta x_d, \Delta y_d\}$. Here, the x-direction is considered as the in-line direction. The survey effort, C, can be defined as a combined attribute of these survey parameters relative to a reference template,

$$\begin{aligned} C &= C_{x_b} \cdot C_{y_b} \cdot C_{x_B} \cdot C_{y_B} \\ &= \frac{\Delta x_{b\mathrm{ref}}}{\Delta x_b} \frac{X_b}{X_{b\mathrm{ref}}} \cdot \frac{\Delta y_{b\mathrm{ref}}}{\Delta y_b} \frac{Y_b}{Y_{b\mathrm{ref}}} \cdot \frac{\Delta x_{B\mathrm{ref}}}{\Delta x_B} x_{rep} \cdot \frac{\Delta y_{B\mathrm{ref}}}{\Delta y_B} y_{rep}, \end{aligned} \tag{1}$$

where $C_{\{\cdot\}}$ is the survey effort for each component, $C_x = C_{x_b} C_{x_B}$, $C_y = C_{y_b} C_{y_B}$, $C_b = C_{x_b} C_{y_b}$, $C_B = C_{x_B} C_{y_B}$, and $C = C_x C_y = C_b C_B$. The subscript 'ref' denotes 'reference'; the factors x_{rep} and y_{rep} are the template-repeat factors resulting from rolling the template in the in-line and the cross-line directions while repeating a part of the template. The attributes in terms of symmetry can be also defined as

$$A_{\Delta x_b} = \frac{\Delta x_b}{\Delta y_b}, \tag{2}$$

$$A_{X_b} = \frac{Y_b}{X_b}, \tag{3}$$

$$A_{\Delta x_B} = \frac{\Delta x_B}{\Delta y_B}, \tag{4}$$

where $A_{\Delta x_b}$ and $A_{\Delta x_B}$ are the aspect ratios of the spatial sampling intervals, and A_{X_b} is the aspect ratio of the spatial sampling apertures. For instance, if a reference template consists of $\{\Delta x_{b\mathrm{ref}}, \Delta y_{b\mathrm{ref}}, X_{b\mathrm{ref}}, Y_{b\mathrm{ref}}, \Delta x_{B\mathrm{ref}}, \Delta y_{B\mathrm{ref}}\} = \{25\,\mathrm{m}, 25\,\mathrm{m}, 6400\,\mathrm{m}, 6000\,\mathrm{m}, 200\,\mathrm{m}, 200\,\mathrm{m}\}$ with $x_{rep} = 1$ and $y_{rep} = 1$, for a template consisting of $\{\Delta x_b, \Delta y_b, X_b, Y_b, \Delta x_B, \Delta y_B\} = \{50\,\mathrm{m}, 50\,\mathrm{m}, 6400\,\mathrm{m}, 6000\,\mathrm{m}, 100\,\mathrm{m}, 100\,\mathrm{m}\}$ with $x_{rep} = 1$ and $y_{rep} = 1$, then $C_x = 1.00$, $C_y = 1.00$, $C_b = 0.25$, $C_B = 4.00$, $C = 1.00$, $A_{\Delta x_b} = 1.00$, $A_{X_b} = 0.94$ and $A_{\Delta x_B} = 1.00$. See e.g. Table 1. These survey parameters and attributes express the specification of seismic data.

Forward model

To describe 3-D seismic data with the survey parameters, the so-called WRW model of Berkhout (1982) is introduced. In this model, discretely sampled 3-D seismic data are described in terms of operator matrices in the space-frequency (xy-f) domain. Each matrix multiplication represents a multi-dimensional spatial convolution. Each element of every matrix contains amplitude and phase information. In this model, seismic data can be described for each monochromatic component as

$$\mathbf{P}\left(z_d, z_s\right) = \mathbf{D}\left(z_d\right) \sum_m \left[\mathbf{W}\left(z_d, z_m\right) \mathbf{R}\left(z_m, z_m\right) \mathbf{W}\left(z_m, z_s\right)\right] \mathbf{S}\left(z_s\right). \tag{5}$$

The various matrices have the following meaning:

- $\mathbf{P}(z_d, z_s)$ is the data matrix of the primary wavefields recorded by detectors at depth z_d due to sources at depth z_s, both depths being close to zero (Figure 1). A row and a column of the data matrix correspond to a certain detector location d at $(\vec{x}_d, z_d) = (x_d, y_d, z_d)$ and a certain source location s at $(\vec{x}_s, z_s) = (x_s, y_s, z_s)$, respectively. For regular spatial sampling, $\Delta x_d = x_{d+1} - x_d$, $\Delta y_d = y_{d+1} - y_d$, $\Delta x_s = x_{s+1} - x_s$ and $\Delta y_s = y_{s+1} - y_s$; see e.g. Figures 1(a) and 1(b). Furthermore, $X_d = \mathrm{Max}(x_d) - \mathrm{Min}(x_d)$, $Y_d = \mathrm{Max}(y_d) - \mathrm{Min}(y_d)$, $X_s = \mathrm{Max}(x_s) - \mathrm{Min}(x_s)$ and $Y_s = \mathrm{Max}(y_s) - \mathrm{Min}(y_s)$, where $\mathrm{Max}(\cdot)$ and $\mathrm{Min}(\cdot)$ are the maximum and the minimum values for each component. According to the row and column numbering, a row $\vec{P}_d^{\dagger}(z_d, z_s)$ constitutes a common-receiver gather, a column $\vec{P}_s(z_d, z_s)$ constitutes a common-source gather, and a submatrix specified by rows for receivers of a receiver line and columns for sources of a source line represents a cross-spread gather. The dagger symbol $\dagger$ is used to denote a row vector. Common-offset gathers and common-mid-point (CMP) gathers are identified in the data matrix as diagonals and anti-diagonals, respectively. An element $P_{ds}(z_d, z_s)$ constitutes one frequency component of a single trace recorded by the d^{th} detector and shot by the s^{th} source, i.e., $P(\vec{x}_d, z_d; \vec{x}_s, z_s; \omega)$.
- $\mathbf{R}(z_m, z_m)$ is the reflectivity matrix representing the conversion of the incident wavefields into the reflected wavefields at depth z_m (Figure 2). In the same manner as the data matrix, a row and a column of the reflectivity matrix correspond to a certain grid-point location i at $(\vec{x}_i, z_m) = (x_i, y_i, z_m)$ and a certain grid-point location j at $(\vec{x}_j, z_m) = (x_j, y_j, z_m)$, respectively. The subscripts i and j indicate variable locations while, later on, the subscript k will be used for a particular location. An element $R_{ij}(z_m, z_m)$ represents one frequency

component of a reflected wavefield at the i^{th} grid point generated by a delta-function source at the j^{th} grid point, i.e., $R(\vec{x}_i, z_m; \vec{x}_j, z_m; \omega)$.

- $\mathbf{S}(z_s)$ is the source matrix, its columns $\vec{S}_s(z_s)$ containing the source properties at $(\vec{x}_s, z_s)$, i.e., $S(\vec{x}_s, z_s; \omega)$.
- $\mathbf{W}(z_m, z_s)$ is the propagation matrix, its columns containing the downgoing wavefields at z_m generated by delta-function sources at z_s. An element of the downgoing wavefields $W_{js}(z_m, z_s)$ represents a direct wavefield at $(\vec{x}_j, z_m)$ caused by a delta-function source at $(\vec{x}_s, z_s)$, i.e., $W(\vec{x}_j, z_m; \vec{x}_s, z_s; \omega)$.
- $\mathbf{W}(z_d, z_m)$ is the propagation matrix, its columns containing the upgoing wavefields at z_d generated by delta-function sources at z_m. An element of the upgoing wavefields $W_{di}(z_d, z_m)$ represents a direct wavefield at $(\vec{x}_d, z_d)$ caused by a delta-function source at $(\vec{x}_i, z_m)$, i.e., $W(\vec{x}_d, z_d; \vec{x}_i, z_m; \omega)$.
- $\mathbf{D}(z_d)$ is the detector matrix, its rows $\vec{D}_d^{\dagger}(z_d)$ containing the detector properties at $(\vec{x}_d, z_d)$, i.e., $D(\vec{x}_d, z_d; \omega)$.

Later on, the spatial coordinate z will sometimes be omitted for brevity. In the case that $\mathbf{W}$ represents one-way wave propagation, Equation (5) can be viewed as the Born approximation to the Lippmann-Schwinger equation with an one-way Green's function $\mathbf{W}$. Equation (5) is a general description of seismic data. In the case of blended acquisition with the blending operator $\mathbf{\Gamma}$, $\mathbf{S\Gamma}$ can replace $\mathbf{S}$ in this equation (Berkhout 2008). For a full-wavefield model, including not only the primary wavefields but also the secondary wavefields generated by surface-related and internal multiples, a full-wavefield propagator or Green's function $\mathbf{G}$ can replace $\mathbf{W}$ in this equation (Kumar *et al.* 2014). Note that with all frequencies the matrices in the frequency domain can be envisaged more naturally in the time domain. Since the discrete Fourier transform is invertible, either domain can be used depending on the purpose. Also note that this forward model is valid for stationary (parts of non-stationary) acquisition geometries.

Double focusing

Double focusing (Berkhout 1997a,b) is the next step leading to the focal-beam method. In this approach, migration can be described in terms of two consecutive focusing steps: focusing in detection and focusing in emission. Focusing in detection is performed by giving each detector signal a phase shift and an amplitude weight such that only one grid point is sensed. Focusing in emission likewise gives each source signal a phase shift and an amplitude weight such that only one grid point is illuminated. Migration should retrieve the reflectivity from the seismic data. Therefore, considering Equation (5), this process can be thought of as removing the effects of the acquisition geometry from the seismic data, i.e., going from **P** to **WRW**, and subsequently removing the effects of wave propagation in the overburden, i.e., going from **WRW** to **R**. Therefore, migration aims at removing **DW** at the detector side and **WS** at the source side for the selected grid point. In the WRW model for a particular depth z_m only, double focusing can be described as

$$\begin{aligned}\hat{R}_{ij}\left(z_m, z_m\right) &= \vec{F}_i^{\dagger}\left(z_m, z_d\right)\mathbf{P}\left(z_d, z_s\right)\vec{F}_j\left(z_s, z_m\right)\\ &= \vec{F}_i^{\dagger}\left(z_m, z_d\right)\mathbf{D}\left(z_d\right)\mathbf{W}\left(z_d, z\right)\\ &\times\mathbf{R}\left(z_m, z_m\right)\\ &\times\mathbf{W}\left(z, z_s\right)\mathbf{S}\left(z_s\right)\vec{F}_j\left(z_s, z_m\right). \end{aligned} \tag{6}$$

Each matrix has the following meaning:

- $\hat{\mathbf{R}}(z_m, z_m)$ is the grid-point matrix or estimated reflectivity matrix at z_m (Figure 2). The hat symbol $\hat{}$ is used to denote 'estimated'. $\hat{R}_{ij}(z_m, z_m)$ is an element of the grid-point matrix.

- $\mathbf{F}(z_m, z_d)$ and $\mathbf{F}(z_s, z_m)$ are the one-way focusing operator removing the wave propagation in the overburden above z_m, or in other words, focusing at z_m from the surface. $\vec{F}_i^{\dagger}(z_m, z_d)$ focuses at the i^{th} grid point at the detector side, and $\vec{F}_j(z_s, z_m)$ focuses at the j^{th} grid point at the source side.

A perfect migration requires $\vec{F}_i^{\dagger}\mathbf{DW} = \vec{I}_i^{\dagger}$ and $\mathbf{WS}\vec{F}_j = \vec{I}_j$, where $\mathbf{I}$ is the identity matrix. In this perfect case, $\hat{R}_{ij}(z_m, z_m)$ is equal to $R_{ij}(z_m, z_m)$. From this concept, survey design can be thought of as choosing $\mathbf{S}$ and $\mathbf{D}$ to obtain a satisfactory migration response, i.e., to obtain a good estimate of $\hat{R}_{ij}(z_m, z_m)$.

~~For *confocal* imaging, in which i is identical to j at a particular location k, i.e., $i = j = k$ in Equation (6) and Figure 2, the angle-averaged reflectivity $\hat{R}_{kk}(z_m, z_m)$ at the k^{th} grid point is obtained.~~ There are two approaches in the double focusing, confocal imaging and bifocal imaging. The confocal imaging results in a scalar image of angle-averaged reflectivity by considering that a certain grid-point location to be focused at the detector side is the same as that at the source side. In this case, i is identical to j at a particular location k, i.e., $i = j = k$ in Equation (6) and Figure 2, and the angle-averaged reflectivity $\hat{R}_{kk}(z_m, z_m)$ at the k^{th} grid point is obtained. ~~Alternatively, for *bifocal* or extended imaging, in which j varies around a particular location k, or vice versa, i.e., $i = k$ and j varying around k, or $j = k$ and i varying around k in Equation (6) and Figure 2, the angle-dependent reflectivity $\hat{\vec{R}}_k^{\dagger}(z_m, z_m)$ or $\hat{\vec{R}}_k(z_m, z_m)$ at the k^{th} grid point is obtained.~~ Alternatively, the bifocal or extended imaging yields a vector image of angle-dependent reflectivity by considering that grid-point locations to be focused at the source side are around a certain grid-point location to be focused at the detector side, or vice versa. In this case, j varies around a particular location k, or vice versa, i.e., $i = k$ and j varying around k, or $j = k$ and i varying around k in Equation (6) and Figure 2, and the angle-dependent reflectivity $\hat{\vec{R}}_k^{\dagger}(z_m, z_m)$ or $\hat{\vec{R}}_k(z_m, z_m)$ at the k^{th} grid point is obtained. This result respects angle-dependent reflectivity information between the incident wavefields and the reflected wavefields. In other words, a plane-wave decomposition of such a result by a linear Radon transform reveals the AVP response (de Bruin *et al.* 1990). Therefore, once the angle-dependent reflectivity is obtained by the bifocal imaging, the AVP response can be obtained by transforming the results to the Radon domain (e.g. Verschuur and Berkhout 2011). This is in contrast with conventional AVP techniques in which the AVP response is obtained by tracking the amplitude change along the reflection in a pre-stack domain. Furthermore, obtaining $\hat{R}_{ij}(z_m, z_m)$ for all frequencies and applying the imaging principle, i.e., imaging at zero time and at zero intercept time, produces results in the spatial (x, y) domain and in the Radon (p_x, p_y) domain, respectively. Note that this idea forms the basis of angle-dependent reflectivity retrieval (MacKay and Abma 1992; Rickett and Sava 2002; Biondi and Symes 2004; Duveneck 2013) and velocity analysis (Shen and Symes 2008; Symes 2008; Mulder 2008, 2014) by means of extended images.

Grid-point decomposition

Seismic data can be viewed as a collection of grid-point responses if a reflector is considered as a series of point diffractors across the reflector. This property makes it possible to perform forward modelling of seismic data and apply double focusing for one or more grid points rather than for the whole subsurface volume. The grid-point decomposition of the data matrix can be described as

$$\mathbf{P}\left(z_d, z_s\right) = \sum_k \delta_k \mathbf{P}\left(z_d, z_s\right), \tag{7}$$

with the grid-point decomposition of the reflectivity matrix as

$$\mathbf{R}\left(z_m, z_m\right) = \sum_k \delta_k \mathbf{R}\left(z_m, z_m\right), \tag{8}$$

where $\delta_k \mathbf{R}(z_m, z_m)$ contains only the response of the k^{th} grid point, and $\delta_k \mathbf{P}(z_d, z_s)$ is obtained with $\delta_k \mathbf{R}(z_m, z_m)$ by Equation (5). The symbol δ is used to emphasize one grid-point diffractor.

For an angle-independent unit-point diffractor at the k^{th} grid point, $\delta_k \mathbf{R}$ contains only one non-zero element, i.e., $\delta_k R_{kk}(z_m, z_m) = 1$ for $i = j = k$, and $\delta_k R_{ij}(z_m, z_m) = 0$ for $i \neq k$ or $j \neq k$, representing the total reflection of the incident wavefield into the reflected wavefield only at the k^{th} grid point.

Focal beams

The focal detector beam is introduced as $\vec{F}_i^{\dagger} \mathbf{D} \mathbf{W}$ at the detector side, and the focal source beam as $\mathbf{W} \mathbf{S} \vec{F}_j$ at the source side in Equation (6). Considering a unit-point diffractor $\delta_k \mathbf{R}$ at the k^{th} grid point, i.e., $\mathbf{R} = \delta_k \mathbf{R}$ in Equation (6), the focal beams contain *angle-dependent* sensing and illumination information that is introduced by the acquisition geometry at the surface, since the reflectivity at the k^{th} grid point in the subsurface has been set to be *angle-independent.* In other words, a plane-wave decomposition of the focal beams by a linear Radon transform reveals angle-dependent sensing and illumination imprints, caused by the source geometry and the detector geometry.

The focal detector beam for a particular depth z_m only (Figures 3(b) and 3(c)) can be described as

$$\vec{D}_k^{\dagger}\left(z_m, z_m\right) = \vec{F}_k^{\dagger}\left(z_m, z_d\right)\mathbf{D}\left(z_d\right)\mathbf{W}\left(z_d, z_m\right). \tag{9}$$

This can be interpreted as a detector array at z_d focused at the k^{th} grid point. Consequently, the focal detector beam contains information predominantly from the detector geometry.

Similar to the focal detector beam, the focal source beam for a particular depth z_m only (Figures 3(e) and 3(f)) can be described as

$$\vec{S}_k\left(z_m, z_m\right) = \mathbf{W}\left(z_m, z_s\right)\mathbf{S}\left(z_s\right)\vec{F}_k\left(z_s, z_m\right). \tag{10}$$

Like the focal detector beam, this can be interpreted as a source array at z_s focused at the k^{th} grid point. As a consequence, the focal source beam contains information predominantly from the source geometry.

Ideally, the focal beams should show a perfect unit-point sensing and illumination (Figure 4(a)), i.e., $\vec{D}_k^{\dagger}(z_m, z_m) = \vec{I}_k^{\dagger}$ and $\vec{S}_k(z_m, z_m) = \vec{I}_k$. In the high-frequency approximation with infinite and dense detector and source coverage, this was proven by Beylkin and Burridge (1990) and ten Kroode *et al.* (1998) and for extended images by ten Kroode (2012). However, this is not the case in practice because of acquisition geometry constraints given by the limited spatial sampling, the limited aperture, and the finite bandwidth of the seismic data. Similarly, the Radon-transformed focal beams should have amplitude spectra uniformly and evenly distributed over all angles (Figure 4(b)). However, this is not the case in practice, again due to acquisition geometry constraints.

In summary, the focal detector beam reveals the sensing capability of the detector geometry and the focal source beam the illumination capability of the source geometry, in terms of spatial resolution in the space domain and pre-stack amplitude fidelity in the Radon domain. These properties offer the opportunity to separately evaluate the detector geometry and the source geometry.

Focal functions

The resolution function (Figure 3(h)) is introduced as a confocal imaging result for a unit-point diffractor $\delta_k\mathbf{R}$ at the k^{th} grid point, i.e., $\mathbf{R} = \delta_k\mathbf{R}$ in Equation (6). The resolution function is defined as the diagonal of the resulting grid-point matrix after double-focusing, i.e., $i = j$ varying around k. The right-hand side of this equation is equivalent to $\vec{F}_i^\dagger\mathbf{D}\mathbf{W}\delta_k\mathbf{R}\mathbf{W}\mathbf{S}\vec{F}_j$. Recall a unit-point response, i.e., $\delta_k R_{kk}(z_m, z_m) = 1$ for $i = j = k$, and $\delta_k R_{ij}(z_m, z_m) = 0$ for $i \neq k$ or $j \neq k$. In this case, for a stationary acquisition geometry, the resolution function can be efficiently obtained by an element-by-element multiplication of the focal detector beam $\vec{D}_k^\dagger(z_m, z_m)$ and the focal source beam $\vec{S}_k(z_m, z_m)$, i.e., the product rule in the space domain (Berkhout *et al.* 2001; van Veldhuizen *et al.* 2008). Ideally, the resolution function should corresponds to a perfect unit-point response in a similar fashion as the focal beams (Figure 4(a)), i.e., $\delta_k\hat{R}_{kk}(z_m, z_m) = 1$ for $i = j = k$, and $\delta_k\hat{R}_{kk}(z_m, z_m) = 0$ for $i \neq k$ or $j \neq k$. However, this hardly occurs in practice due to acquisition geometry constraints. Fortunately, because of the product rule, deficiencies in the focal detector beam are often compensated for by the focal source beam, or vice versa, possibly resulting in a satisfactory resolution function.

The AVP function (Figure 3(i)) is introduced as a bifocal imaging result for an angle-independent unit reflector $\Delta\mathbf{R}$ including the k^{th} grid point, i.e., $\mathbf{R} = \Delta\mathbf{R}$ in Equation (6). The symbol Δ is used to denote one single reflector. The right-hand side of this equation is equivalent to $\vec{F}_i^\dagger\mathbf{D}\mathbf{W}\Delta\mathbf{R}\mathbf{W}\mathbf{S}\vec{F}_j$. Notice a unit-reflector response, i.e., $\Delta\mathbf{R} = \mathbf{I}$. In this case, for a stationary acquisition geometry, the AVP function can be approximated by a convolution of the focal detector beam $\vec{D}_k^\dagger(z_m, z_m)$ and the focal source beam $\vec{S}_k(z_m, z_m)$ and, therefore, by an element-by-element multiplication of the Radon-transformed focal detector beam and the Radon-transformed focal source beam, i.e., the product rule in the Radon domain as defined by Berkhout *et al.* (2001) and mathematically proven by van Veldhuizen *et al.* (2008). Ideally, the AVP function should have amplitude spectra uniformly and evenly distributed over all angles in a similar fashion as the Radon-transformed focal beams (Figure 4(b)). However, this seldom occurs in practice, again due to acquisition geometry constraints. In this case, the AVP function reveals the angle-dependent imprint caused by both the source geometry and the detector geometry.

In summary, the resolution function reveals the achievable spatial resolution in the space domain, and the AVP function shows the achievable pre-stack amplitude fidelity in the Radon domain, both for the total acquisition geometry, i.e., the combination of the detector geometry and the source geometry. These properties offer the opportunity to optimize the acquisition geometry in order to efficiently maximize the spatial resolution and to effectively minimize the AVP imprint.

Survey evaluation and design using the focal-beam method

The focal-beam method enables survey evaluation and design. In this approach, the input information comprises an acquisition geometry at the surface, a subsurface model with the macro-velocities including one or more target grid points in the subsurface, and a focusing operator. With this information, the focal beams and the focal functions can be computed. For a non-stationary acquisition geometry, e.g., with rolls in inline and crossline directions, the partial focal beams and the partial focal functions are computed for each stationary part. Then, the total focal beams and the total focal functions are obtained by summation of the partial ones (Figures 3(k) and 3(l)). Note that the focal-beam method is most efficient for an acquisition geometry with large stationary parts such as 3-D OBC/OBN seismic surveys. With the focal beams and the focal functions, certain attributes can be quantitatively analysed, for instance, the achievable resolution and pre-stack amplitude fidelity, in particular the strength and width of the focusing result in the space domain and the spectral bandwidth and flatness of the focusing result in the Radon domain. In this way, the given acquisition geometry can then be evaluated against the required data quality for imaging and AVP applications of the target reflectors.

A CASE STUDY OFFSHORE ABU DHABI

We applied the focal-beam method to several acquisition geometries (Table 1) for 3-D shallow-water seismic survey evaluation and design offshore Abu Dhabi. The abbreviation 'OR' stands for 'orthogonal', and 'AR' for 'areal'. In the region, earlier studies suggested some attributes required to image the target reflectors (Ishiyama *et al.* 2010c): a trace density, i.e., nominal fold per bin size, of about $1.5\,/\mathrm{m}^2$; a maximum offset, i.e., half of a maximum aperture, of about 3800 m corresponding to a maximum inline offset of about 3200 m with the 85 % rule (Cordsen *et al.* 2000). The acquisition geometries in Table 1 satisfy these criteria. Notice that in all cases the trace density and the survey effort are equally constant, i.e., $\rho_{bin} = 1.54\,/\mathrm{m}^2$ and $C = 1$. For the subsurface model, the layered P-wave and S-wave velocity models were built from well log data in the region. The target grid point was set at a depth level of the Upper Jurassic formations and at the center of a horizontal area of 8 km × 8 km. The average P-wave velocity around the target level is about 4 km/s, the interval P-wave velocity about 6 km/s, and the interval S-wave velocity about 3.2 km/s. For the wave propagation operator, recursive and explicit one-way extrapolation operators (e.g. Blacquière *et al.* 1989; Thorbecke *et al.* 2004) were used both for the forward modelling and for the double focusing. The focal beams and the focal functions were computed up to a maximum frequency of 50 Hz.

Effects of spatial sampling intervals with the symmetry

Figure 5 shows the results from three acquisition geometries: OR1144, OR2222 and OR4411 in Table 1, which have the same spatial sampling apertures but different intervals. These are orthogonal geometries in which the receiver lines are deployed in the x-direction whereas the source lines are oriented in the y-direction. These acquisition geometries almost meet the symmetric sampling criterion: the receiver-point interval is equal to the source-point interval, $\Delta x_b = \Delta y_b$ and $A_{\Delta x_b} = 1$, the receiver-line interval is identical to the source-line interval, $\Delta x_B = \Delta y_B$ and $A_{\Delta x_B} = 1$, and the receiver-line length is almost the same as the source-line length, $X_B \approx Y_B$ and $A_{X_b} \approx 1$. Figures 5(a) show the acquisition geometry spreads, where blue triangles and red circles indicate receivers and sources, respectively.

Figures 5(b) and 5(c) show the focal detector beams in the space domain and in the Radon domain, respectively. In the space domain, the axes are the x- and y-distances from the target grid point. In the Radon domain, the axes indicate the ray-parameters p_x and p_y related to the target grid point. The maximum of the axes is the slowness at the target grid point, i.e., the inverse of the interval velocity with an angle of 90 degrees. The colour scale represents the normalized amplitude. In the space domain, a well-focused lobe is found at the target grid point for all three cases, because of adequate spatial sampling apertures. However, some aliasing effects are present in the y-direction for OR1144 and OR2222 due to the coarse spatial sampling interval in this direction. In the Radon domain, a broad range of angles is seen for all three cases because of the high aspect ratio of the apertures. However, some band-like features exist with a periodicity in the y-direction for OR1144 and OR2222 due to the aliasing effects. OR4411 shows no obvious deficiency, because of the relatively fine sampling in both the x- and y-directions. Figures 5(d) and 5(e) show the focal source beams. The same observations can be made but in the other direction, i.e., in the x-direction in this case.

Figures 5(f) and 5(~~h~~g) show the resolution functions and the AVP functions, respectively. For the resolution function, a well-focused lobe is found only at the target grid point and no aliasing effect is observed away from it for all three cases. This is because the aliasing effects occur in two orthogonal directions, i.e., in the y-direction for the focal detector beam and in the x-direction for the focal source beam. These effects are canceled by the product rule for the resolution function. Because of the product rule, the deficiencies in the focal detector beam are compensated for by the focal source beam, or vice versa, and this results in the satisfactory resolution function. This explains why most common acquisition geometries achieve a quite acceptable resolution. In fact, this agrees with the suggestion of Vermeer

(2010) that proper spatial sampling for imaging implies proper sampling of two of the four spatial coordinates. The results show that the resolution function is robust against the aliasing effects and that the resolution is not much affected by the acquisition geometry, if the detector geometry and the source geometry have different coarse sampling directions and if their apertures are adequate. This means that the spatial sampling intervals and apertures of the basic subset, Δx_b, Δy_b, X_b and Y_b, are the essential types of survey parameters for reflection imaging. For the AVP function, AVP imprints related to the acquisition geometry are clearly seen for OR1144 and OR2222. This is because the aliasing effects expanded over angles, both for the focal detector beam and the focal source beam, are intensified by the product rule for the AVP function. This is not the case for OR4411 because of no obvious deficiency in either the focal detector beam or the focal source beam. These results show that the AVP imprints are sensitive to the aliasing effects and that the pre-stack amplitude fidelity is easily affected by the acquisition geometry. To obtain the ideal AVP function, proper sampling of all four spatial coordinates may be required, although this condition is obviously demanding. This means that all the four spatial sampling intervals and apertures of the template geometry, Δx_b, Δy_b, X_b, Y_b Δx_B and Δy_B, are essential for AVP applications.

Effects of spatial sampling intervals with the asymmetry

We now compare the results from six acquisition geometries: OR4122, OR2222, OR2241, AR284Q, AR244H and AR2241 in Table 1, which have the same spatial sampling apertures, but again different intervals. OR4122 has a receiver-point interval differing from the source-point interval, OR2241 has a receiver-line interval differing from the source-line interval and, therefore, they are asymmetric. AR284Q, AR244H and AR2241 are areal geometries to be acquired with parallel swath shooting in which the receiver lines and the source lines are parallel in the x-direction. The receivers are arranged sparsely in the y-direction while the sources are on a densely spaced grid, and therefore, these are asymmetric. From the four spatial coordinates point of view, OR2241 and AR2241 are equivalent.

The results in Figure 6 exhibit the acquisition geometry spreads and the focal functions.

For the resolution function, a well-focused lobe is found only at the target grid point and no aliasing effect is observed away from it for all six cases. These results again show the robustness of the resolution function, regardless of the asymmetry. For the AVP function, OR4122 and OR2222 show subtle AVP imprints. However, others display severe band-like features with a periodicity in the coarse sampling direction, i.e., in the y-direction in this case. These results show that the AVP spectral flatness depends on the sparsity of the acquisition geometry and is severely affected in the coarse sampling direction, regardless of the asymmetry and the acquisition geometry type.

Effects of spatial sampling apertures and the symmetry

Figure 7 shows the results of OR2222 in Table 1. Now, the three cases have different spatial sampling apertures, roll patterns and resulting aspect ratios of the apertures: OR2222, OR2222_10R5 and OR2222_10R5_SLI. Generic choices for the OBC/OBN acquisition geometry are made: a 10-roll-5 receiver-line roll whereby 10 receiver lines are active in the current patch while 5 extra receiver lines are rolled from the previous patch to the following patch in the crossline direction during the shooting in the current patch; a source-line interleave whereby source lines in a patch are interleaved by source lines from the previous and following patches (Ishiyama *et al.* 2012). OR2222_10R5 adopts 10-roll-5 receiver-line roll, a patch of which has a crossline aperture and an aspect ratio of half those of OR2222. OR2222_10R5_SLI corresponds to OR2222_10R5 with the source-line interleave, a patch of which has the same crossline aperture and aspect ratio as those of OR2222. Both of them cover the whole surface area by five rolls in this case.

The results in Figure 7 exhibit the patch spreads of the acquisition geometries and the focal functions. For the resolution function, the same observations can be made in all three cases. For the AVP function, OR2222 and OR2222_10R5_SLI show a broad expanse, although OR2222_10R5_SLI has reasonable but no extra dilation in the crossline direction. Besides, OR2222_10R5 displays a limited bandwidth in the crossline direction, i.e., in the y-direction in this case. These results show that the AVP spectral bandwidth depends on the spatial sampling aperture in the crossline direction and the resulting aspect ratio of the apertures, and is constrained by the shorter aperture in the crossline direction, regardless of the acquisition geometry type and roll pattern.

Effects of wave types to be recorded

Figure 8 shows the results of OR2222 in Table 1. Now, the three cases have different wave types to be recorded: OR2222, OR2222_PS and OR2222_SS. Using converted waves is a natural and interesting option, since one of the advantages of OBC/OBN seismic surveys is a direct S-wave measurement by a 4-C receiver, although these waves have not yet been fully utilized in the region today. For the P-S wave, the conversion from P-wave to S-wave is assumed to occur at the target grid point during the reflection. The focal source beam is computed with the P-wave velocity model, the focal detector beam with the S-wave velocity model, and these focal beams are straightforwardly combined to obtain the focal functions. For the (P-)S-S wave, a conversion from P-wave to S-wave is supposed to occur near the surface. In the region, a dominant mode conversion to S-wave near the surface exists because of the very shallow-water depth and the hard sea bottom. These events are confirmed in existing seismic data recorded by horizontal component geophones (Berteussen and Sun 2010). In this case, both the focal beams and the focal functions are computed with the S-wave velocity model.

The results in Figure 8 exhibit the focal beams and the focal functions. For the focal beams, the same observations can be made as in the previous examples except for the range of ray-parameters for S-waves. The maximum ray-parameter for an S-wave is much larger than that for a P-wave because of the lower interval velocity at the target grid point. The maximum ray-parameter in the axes for a P-wave corresponds to 90 degrees in angle and is comparable with about 30 degrees for an S-wave and, therefore, wider extents of ray-parameters for the focal detector beam of OR2222_PS and for both the focal detector beam and the focal source beam of OR2222_SS are found. However, for OR2222_PS, the attainable extent is limited by the aperture of the source geometry. To fully acquire the extent of ray-parameter, a wider aperture of the source geometry would be required. For the resolution function, OR2222_PS and OR2222_SS show a sharper resolution because of the shorter S-wave length. However, for the AVP function, OR2222_PS and OR2222_SS display more severe AVP imprints due to the stronger aliasing effects caused by the lower S-wave velocity while keeping the spatial sampling intervals the same. These results show that the resolution function improves, however, AVP imprints become seemingly worse when utilizing the converted waves. To obtain the ideal AVP function, a much finer sampling of the four spatial coordinates would be required. However, AVP applications for seismic reservoir characterization using jointly P-waves and converted waves are more robust than those using only P-waves even for a limited range of ray-parameter and more severe AVP imprints (van Veldhuizen *et al.* 2008). Therefore, much finer sampling may not always be required for utilizing converted waves.

DISCUSSION

Based on the case study, the relationship between the survey parameters and the resulting data quality for reflection imaging and AVP applications is described as

- Resolution is robust and not much affected by the aliasing effects introduced by the acquisition geometry if it has two different fine-sampling directions while satisfying the required apertures. At least two of the four spatial coordinates should be sampled densely, and the other coordinates can be sampled in an affordable manner. This means that the spatial sampling intervals and apertures of the basic subset, Δx_b, Δy_b, X_b and Y_b, are essential for reflection imaging.
- Pre-stack amplitude fidelity is sensitive to and easily affected by the aliasing effects. First, the AVP spectral flatness is severely affected in the coarse sampling direction, regardless of the symmetry, the asymmetry and the acquisition geometry type. The sparsity should not be thrust into a particular sampling direction, but should be shared by all four spatial coordinates. Second, the AVP spectral bandwidth is constrained by the shorter aperture in the crossline direction, regardless of the acquisition geometry type and roll pattern. The

aspect ratio should be close to one while satisfying the required apertures. This means that all the four spatial sampling intervals and apertures of the template geometry, Δx_b, Δy_b, X_b, Y_b Δx_B and Δy_B, are essential for AVP applications.

- Resolution improves, but pre-stack amplitude fidelity ostensibly deteriorates when utilizing converted waves while keeping the four spatial sampling the same, i.e., based on P-wave properties. However, the required pre-stack amplitude fidelity can be relaxed because of the robustness of seismic reservoir characterization using P-waves and converted waves jointly.

In this paper, we considered the capability of an acquisition geometry that enables imaging and AVP applications of target reflectors. However, in the region, seismic data are often dominated by surface waves masking the reflections. They impose additional requirements on the acquisition geometry, since it should allow for effective surface-wave separation or removal (Berteussen *et al.* 2011). We recently discussed the essential types of survey parameters for surface-wave separation using signal-to-noise ratio (SNR) as an attribute representing the resulting data quality. We observed that the spatial sampling intervals of the basic subset, Δx_b and Δy_b, are essential in terms of surface-wave separation (Ishiyama *et al.* 2014). Figure 9 illustrates which types of survey parameters are essential for surface-wave separation, reflection imaging and AVP applications, respectively. Notice that the parameters Δx_b and Δy_b, in the lower left of the figure, are essential for surface-wave separation but also for reflection imaging and AVP applications. If these parameters are satisfactory for a required SNR given for the first, they usually also provide sufficient data quality for the others. This is because surface waves often correspond to a lower velocity than reflections, and are more aliased.

Recently, the concept of random spatial sampling followed by data reconstruction has been introduced in survey design, which extracts broader spatial bandwidth from seismic data than that expected by the Nyquist criterion (e.g. Hennenfent and Herrmann 2008; Herrmann 2010). If reflection imaging and AVP applications are applied directly to the irregularly and under-sampled seismic data, an optimal acquisition geometry, e.g., **S** and **D** with irregularly and sparsely distributed sources and receivers, can be found by the focal-beam method. However, migration often gives best results for regularly and densely sampled seismic data (Vermeer 2010). Therefore, seismic data should be regularized and interpolated prior to applying migration. This imposes additional requirements on the acquisition geometry so that those can allow for effective regularization and interpolation. Milton *et al.* (2011) suggested that the requirements are evenly but randomly distributed sources and receivers with avoiding large gaps and severe aliasing. Moldoveanu (2010) and Mosher *et al.* (2012) suggested finding the optimal acquisition geometry using an optimization-loop or iterative approach based on the so-called compressive sensing in the field of applied mathematics. This may correspond to finding spatially averaged values of the survey parameters in Figure 9, e.g., $\overline{\Delta x_b}$, $\overline{\Delta y_b}$, $\overline{X_b}$, $\overline{Y_b}$, $\overline{\Delta x_B}$ and $\overline{\Delta y_B}$, using a certain attribute or measure representing the resulting data quality after regularization and interpolation. Here, the over-line $\bar{\cdot}$ indicates 'on average'. This development is of great interest but beyond the scope of this paper.

CONCLUSIONS

We applied the focal-beam method to 3-D shallow-water seismic survey evaluation and design offshore Abu Dhabi. Reviewing the results from several acquisition geometries, the capability of acquisition geometry is described as follows.

- The spatial sampling intervals and apertures of the basic subset are the essential types of survey parameters for reflection imaging.
- All the four spatial sampling intervals and apertures of the template geometry are the essential types of survey parameters for AVP applications.
- The spatial sampling intervals of the basic subset are essential for surface-wave separation. Suitable spatial sampling intervals for surface-wave separation also suffice for reflection imaging and AVP applications.

Therefore, given a required data quality, optimal values of these essential types of survey parameters can be found based on the relationship between the survey parameters and the resulting data quality.

ACKNOWLEDGMENTS

We thank Adnoc and their R&D Oil Sub-Committee for their permission to use the data offshore Abu Dhabi and publish this paper. We acknowledge Inpex for their financial support for this research. We are grateful to the Delphi consortium sponsors for their support and discussions on this research. We also thank Wim Mulder and anonymous reviewers for ~~his review and~~their constructive comments to improve this paper.

REFERENCES

Berkhout, A. J., 1982. *Seismic migration, imaging of acoustic energy by wavefield extrapolation, A. Theoretical aspects*, Elsevier.

Berkhout, A. J., 1997. Pushing the limits of seismic imaging, Part I: Prestack migration in terms of double dynamic focusing, *Geophysics*, **62**, 937–953.

Berkhout, A. J., 1997. Pushing the limits of seismic imaging, Part II: Integration of prestack migration, velocity estimation, and AVO analysis, *Geophysics*, **62**, 954–969.

Berkhout, A. J., 2008. Changing the mindset in seismic data acquisition, *The Leading Edge*, **27**(6), 924–938.

Berkhout, A. J., Ongkiehong, L., Volker, A. W. F., and Blacquière, G., 2001. Comprehensive assessment of seismic acquisition geometries by focal beams – Part I: Theoretical considerations, *Geophysics*, **66**, 911–917.

Berteussen, K. and Sun, Y., 2010. Multicomponent seismic acquisition in the Arabic Gulf – Should we take a new look at the acquisition parameters, *72nd EAGE Conference & Exhibition Extended Abstracts*.

Berteussen, K., Zhang, Z., and Sun, Y., 2011. Surface wave analysis of Arabian Gulf ocean bottom seismic data, *73rd EAGE Conference & Exhibition Extended Abstracts*.

Beylkin, G. and Burridge, R., 1990. Linearized inverse scattering problems in acoustics and elasticity, *Wave Motion*, **12**, 15–52.

Biondi, B. and Symes, W. W., 2004. Angle-domain common-image gathers for migration velocity analysis by wavefield-continuation imaging, *Geophysics*, **69**, 1283–1298.

Blacquière, G., Debeya, H. W. J., Wapenaar, C. P. A., and Berkhout, A. J., 1989. 3D table-driven migration, *Geophys. Prosp.*, **37**, 925–958.

Cordsen, A., Galbraith, M., and Peirce, J., 2000. *Planning land 3-D seismic surveys*, Soc. Expl. Geophys.

de Bruin, C. G. M., Wapenaar, C. P. A., and Berkhout, A. J., 1990. Angle-dependent reflectivity by means of prestack migration, *Geophysics*, **55**, 1223–1234.

Duveneck, E., 2013. A pragmatic approach for computing full-volume RTM reflection angle/azimuth gathers, *75th EAGE Conference & Exhibition Extended Abstracts*.

Galbraith, M., 2004. A new methodology for 3D survey design, *The Leading Edge*, **23**(10), 1017–1023.

Hennenfent, G. and Herrmann, F. J., 2008. Simply denoise: Wavefield reconstruction via jittered undersampling, *Geophysics*, **73**, V19–V28.

Herrmann, F. J., 2010. Randomized sampling and sparsity: Getting more information from fewer samples, *Geophysics*, **75**, WB173–WB187.

Ishiyama, T., Ikawa, H., and Belaid, K., 2010. AVO applications for porosity and fluid estimation of carbonate reservoirs offshore Abu Dhabi, *First Break*, **28**(2), 93–100.

Ishiyama, T., Ikawa, H., Painter, D., and Belaid, K., 2010. Multi-azimuth processing and its applications to wide-azimuth OBC seismic data offshore Abu Dhabi, *First Break*, **28**(6), 43–52.

Ishiyama, T., Painter, D., and Belaid, K., 2010. 3D OBC seismic survey parameters optimization offshore Abu Dhabi, *First Break*, **28**(11), 39–46.

Ishiyama, T., Mercado, G., and Belaid, K., 2012. 3D OBC seismic survey geometry optimization offshore Abu Dhabi, *First Break*, **30**(1), 51–59.

Ishiyama, T., Blacquière, G., and Mulder, M. A., 2014. The impact of surface-wave separation of 3-D seismic survey design, *Geophys. Prosp.*, p. Submitted.

Kumar, A., Blacquière, G., and Verschuur, D. J., 2014. 3D acquisition geometry analysis: incorporating information from multiples, *84th SEG Annual Meeting Technical Program Expanded Abstracts*, **33**, 30–35.

MacKay, S. and Abma, R., 1992. Imaging and velocity analysis with depth-focusing analysis, *Geophysics*, **57**, 1608–1622.

Milton, A., Trickett, S., and Burroughs, L., 2011. Reducing acquisition costs with random sampling and multidimensional interpolation, *81st SEG Annual Meeting Technical Program Expanded Abstracts*, **30**, 52–56.

Moldoveanu, N., 2010. Random sampling: A new strategy for marine acquisition, *80th SEG Annual Meeting Technical Program Expanded Abstracts*, **29**, 51–55.

Mosher, C. C., Kaplan, S. T., and Janiszewski, F. D., 2012. Non-uniform optimal sampling for seismic survey design, *74th EAGE Conference & Exhibition Extended Abstracts*.

Mulder, W. A., 2008. Automatic velocity analysis with the two-way wave equation, *70th EAGE Conference & Exhibition Extended Abstracts*.

Mulder, W. A., 2014. Subsurface offset behaviour in velocity analysis with extended reflectivity images, *Geophys. Prosp.*, **62**, 17–33.

Nakayama, S., Belaid, K., and Ishiyama, T., 2013. Seeking efficient OBC survey designs that still satisfy established geophysical objectives, *First Break*, **31**(10), 65–73.

Ren, H., Wu, R., and Wang, H., 2011. Wave equation least square imaging using the local angular hessian for amplitude correction, *Geophys. Prosp.*, **59**, 651–661.

Rickett, J. E. and Sava, P. C., 2002. Offset and angle-domain common image-point gathers for shot-profile migration, *Geophysics*, **67**, 883–889.

Shen, P. and Symes, W. W., 2008. Automatic velocity analysis via shot profile migration, *Geophysics*, **73**, VE49–VE59.

Symes, W. W., 2008. Migration velocity analysis and waveform inversion, *Geophys. Prosp.*, **56**, 765–790.

ten Kroode, A. P. E., 2012. A wave-equation-based Kirchhoff operator, *Inverse Problems*, **28**, 115013.

ten Kroode, A. P. E., Smit, D. J., and Verdel, A. R., 1998. A microlocal analysis of migration, *Wave Motion*, **28**, 149–172.

Thorbecke, J. W., Wapenaar, C. P. A., and Swinnen, G., 2004. Design of one-way wavefield extrapolation operators, using smooth functions in WLSQ optimization, *Geophysics*, **69**, 1037–1045.

van Veldhuizen, E. J., Blacquir̀e, G., and Berkhout, A. J., 2008. Acquisition geometry analysis in complex 3D media, *Geophysics*, **73**, Q43–Q58.

Vermeer, G. J. O., 2010. 3D symmetric sampling of sparse acquisition geometries, *Geophysics*, **75**, WB3–WB14.

Vermeer, G. J. O., 2012. *3-D seismic survey design*, Soc. Expl. Geophys.

Verschuur, D. J. and Berkhout, A. J., 2011. Seismic migration of blended shot records with surface-related multiple scattering, *Geophysics*, **76**, A7–A13.

Volker, A. W. F., Blacquière, G., Berkhout, A. J., and Ongkiehong, L., 2001. Comprehensive assessment of seismic acquisition geometries by focal beams – Part II: Practical aspects and examples, *Geophysics*, **66**, 918–931.

Wei, W., Fu, L., and Blacquière, G., 2012. Fast multifrequency focal beam analysis for 3D seismic acquisition geometry, *Geophysics*, **77**, P11–P21.

LIST OF FIGURES

5 (Continued) (e) the focal source beams in the Radon domain; (f) the zoomed-in images of the resolution functions in the space domain; (g) the AVP functions in the Radon domain. Blue and red in a geometry spread indicate receiver and source locations. Colour scales of focal beams and focal functions represent normalized amplitudes.

6 The acquisition geometry spread and focal functions of OR4122 (1^{st} column), OR2222 (2^{nd} column) and OR2241 (3^{rd} column). (a) The geometry spreads around the center; (b) the zoomed-in images of the resolution functions in the space domain; (c) the AVP functions in the Radon domain. (to be continued)

6 (Continued) The acquisition geometry spread and focal functions of AR284Q (4^{th} column), AR244H (5^{th} column) and AR2241 (6^{th} column). (a) The geometry spreads around the center; (b) the zoomed-in images of the resolution functions in the space domain; (c) the AVP functions in the Radon domain. Blue and red in a geometry spread indicate receiver and source locations. Colour scales of focal beams and focal functions represent normalized amplitudes.

7 A stationary part of the acquisition geometry and the total focal functions of OR2222_10R5 (1^{st} column), OR2222 (2^{nd} column) and OR2222_10R5_SLI (3^{rd} column). (a) The patch spreads; (b) the zoomed-in images of the resolution functions in the space domain; (c) the AVP functions in the Radon domain. Blue and red in a geometry spread indicate receiver and source locations. Colour scales of focal beams and focal functions represent normalized amplitudes.

8 The focal beams and focal functions of OR2222_PS (1^{st} column), OR2222 (2^{nd} column) and OR2222_SS (3^{rd} column). (a) the focal detector beams in the space domain; (b) the focal detector beams in the Radon domain; (c) the focal source beams in the space domain; (d) the focal source beams in the Radon domain; (to be continued)

8 (Continued) (e) the zoomed-in images of the resolution functions in the space domain; (f) the cross sections of the dashed lines on the above; (g) the AVP functions in the Radon domain. Colour scales of focal beams and focal functions represent normalized amplitudes.

9 The essential types of survey parameters for surface-wave separation, reflection imaging and AVP applications. Survey parameters should be determined from the lower left to the upper right in the figure.

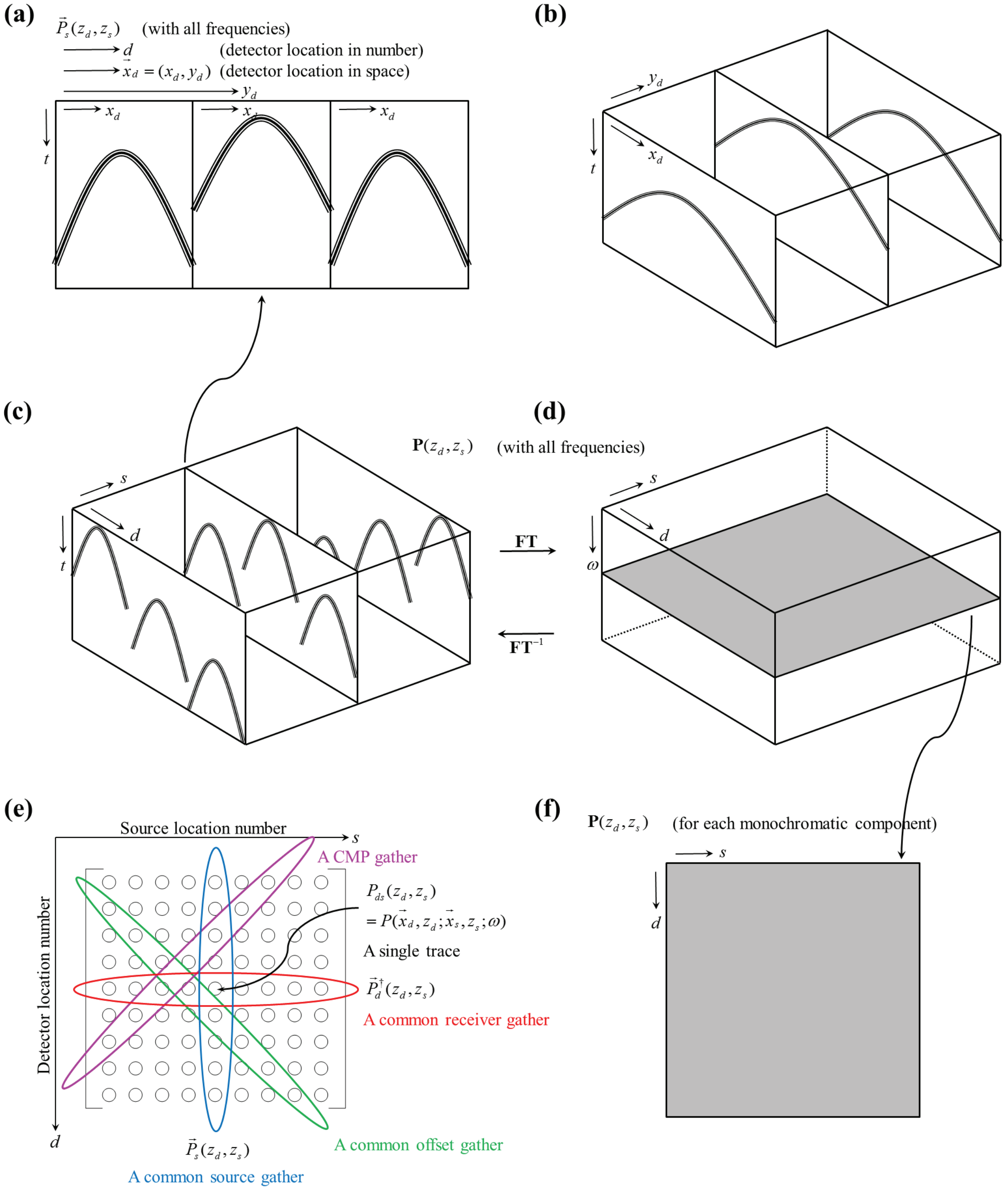

Figure 1. A common-source gather $\vec{P}_s(z_d,z_s)$ for a certain source s at $\vec{x}_s$ with all frequencies, (a) in the 2-D d-t domain, and (b) in the 3-D xy-t domain. A common-receiver gather $\vec{P}_d^{\dagger}(z_d,z_s)$ can be considered in the same way but for a certain detector d at $\vec{x}_d$. Seismic data $\mathbf{P}(z_d,z_s)$ with all frequencies, (c) in the 3-D ds-t domain, and (d) in the 3-D ds-ω domain, are described by (e) and (f) data matrix $\mathbf{P}(z_d,z_s)$ for each monochromatic component.

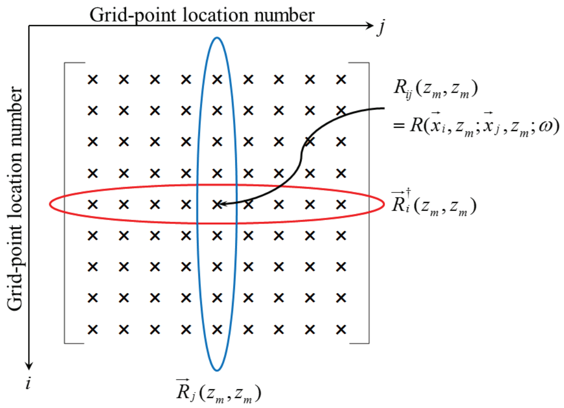

Figure 2. Schematic reflectivity matrix $\mathbf{R}(z_m, z_m)$ for each monochromatic component.

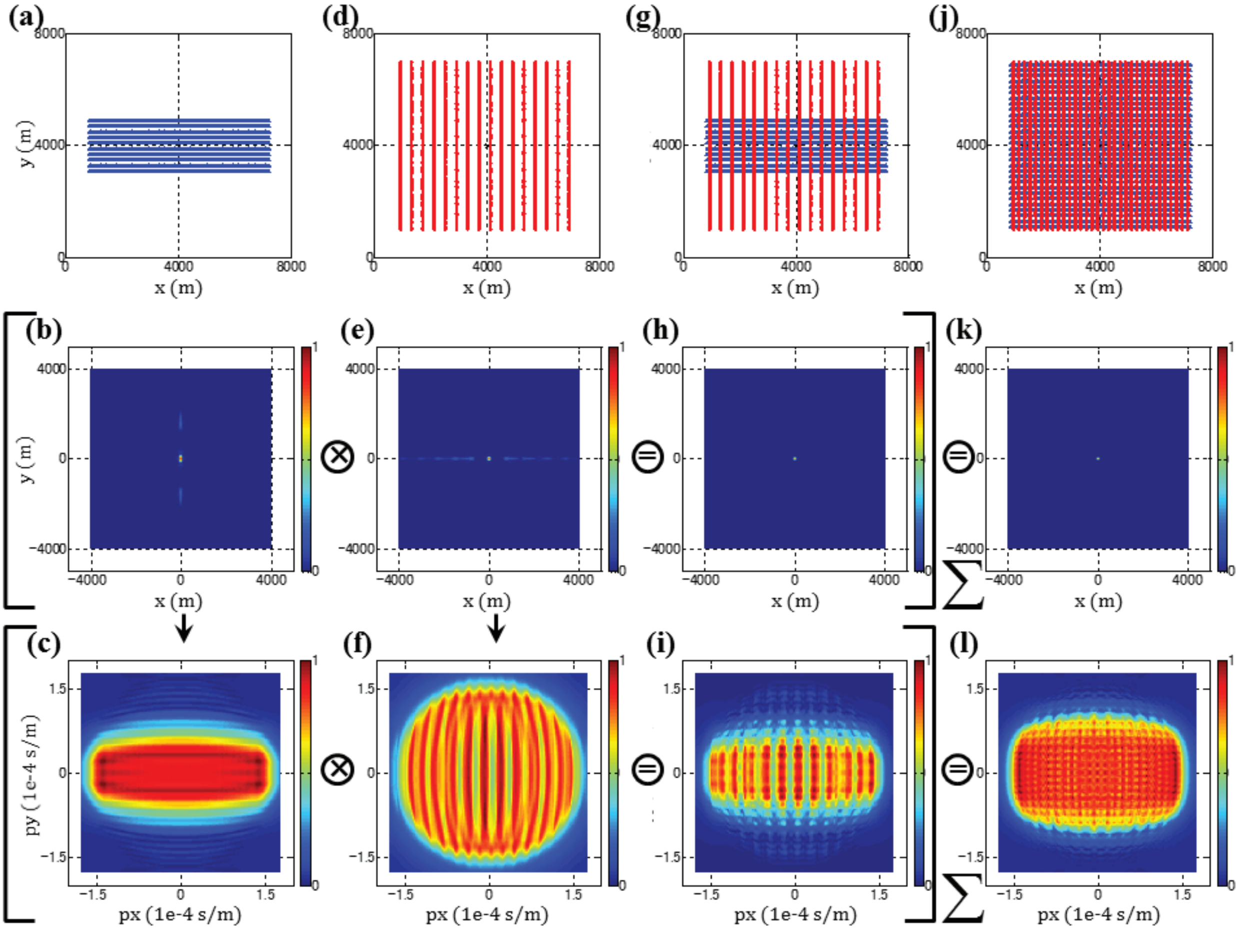

Figure 3. Focal detector beams (1^{st} column), focal source beams (2^{nd} column), focal functions (3^{rd} column) for a stationary part of acquisition geometry, and total focal functions (4^{th} column) for the whole of acquisition geometry that is covered by five rolls in the crossline direction. (a), (d), (g) and (j) The geometry spreads; (b), (e), (h) and (k) the focal beams and resolution functions in the space domain; (c), (f), (i) and (l) the focal beams and AVP functions in the Radon domain. Blue and red in a geometry spread indicate receiver and source locations. Colour scales of focal beams and focal functions represent normalized amplitudes.

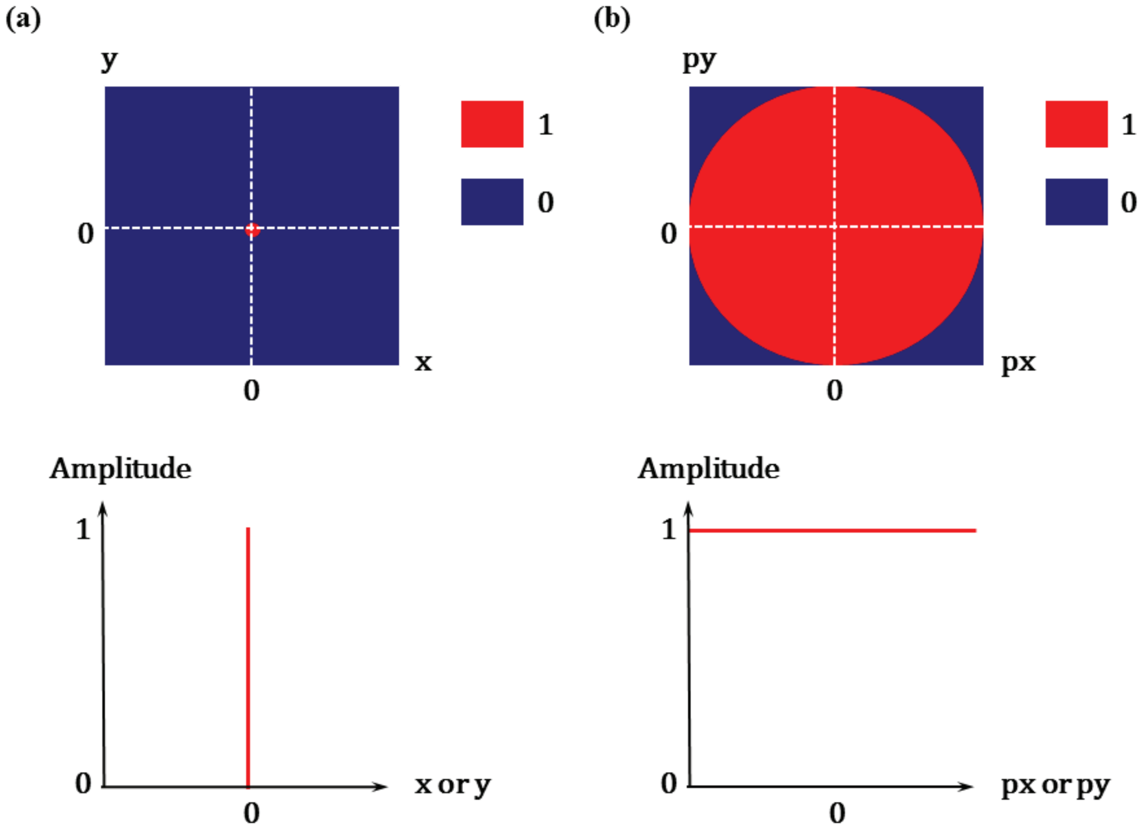

Figure 4. The ideal situation of focal beams and focal functions on the maps (top) and the cross sections of the dashed lines on the maps (bottom), (a) in the space domain, and (b) in the Radon domain.

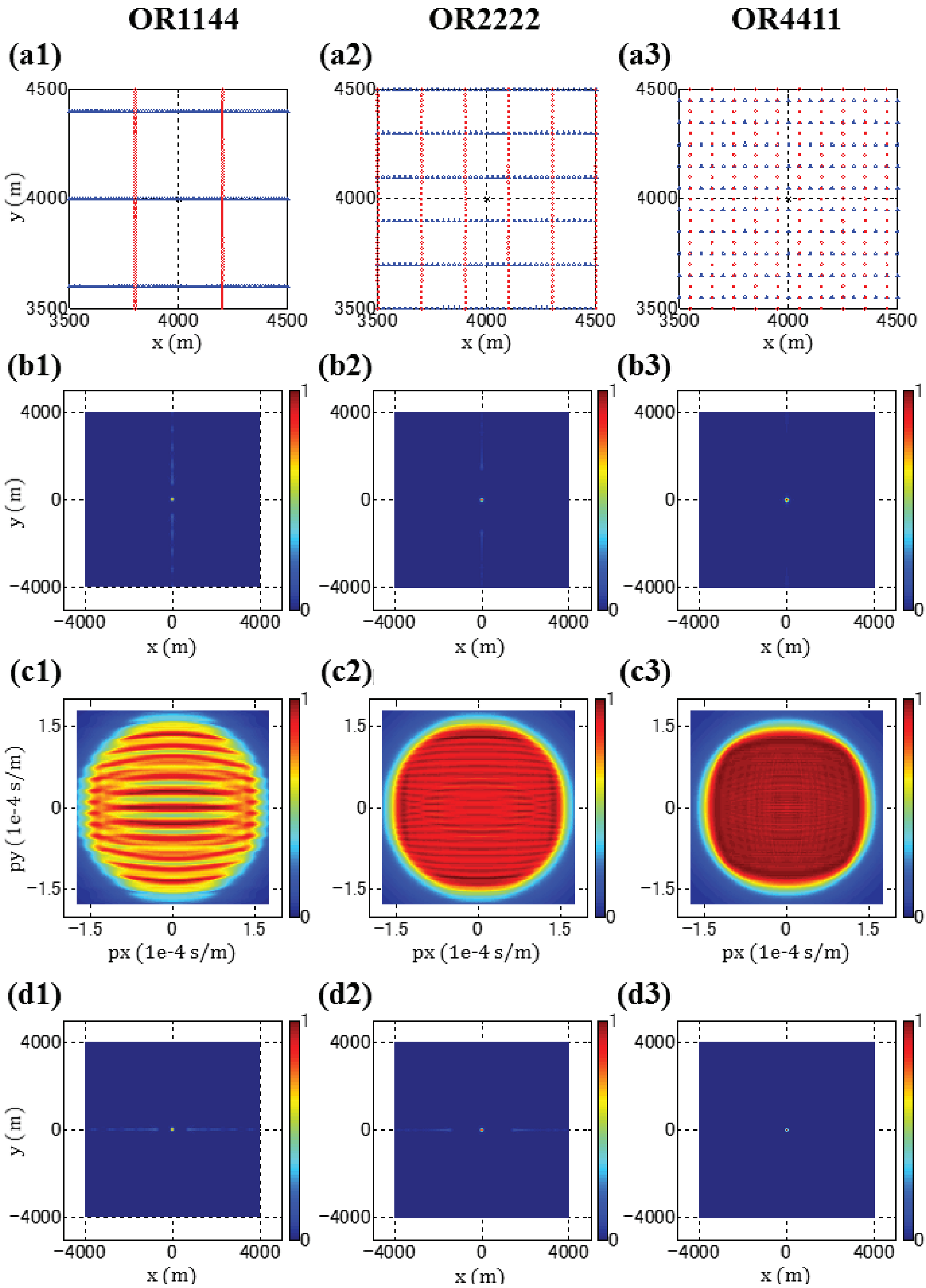

Figure 5. The acquisition geometry spread, focal beams and focal functions of OR1144 (1^{st} column), OR2222 (2^{nd} column) and OR4411 (3^{rd} column). (a) The geometry spreads around the center; (b) the focal detector beams in the space domain; (c) the focal detector beams in the Radon domain; (d) the focal source beams in the space domain; (to be continued)

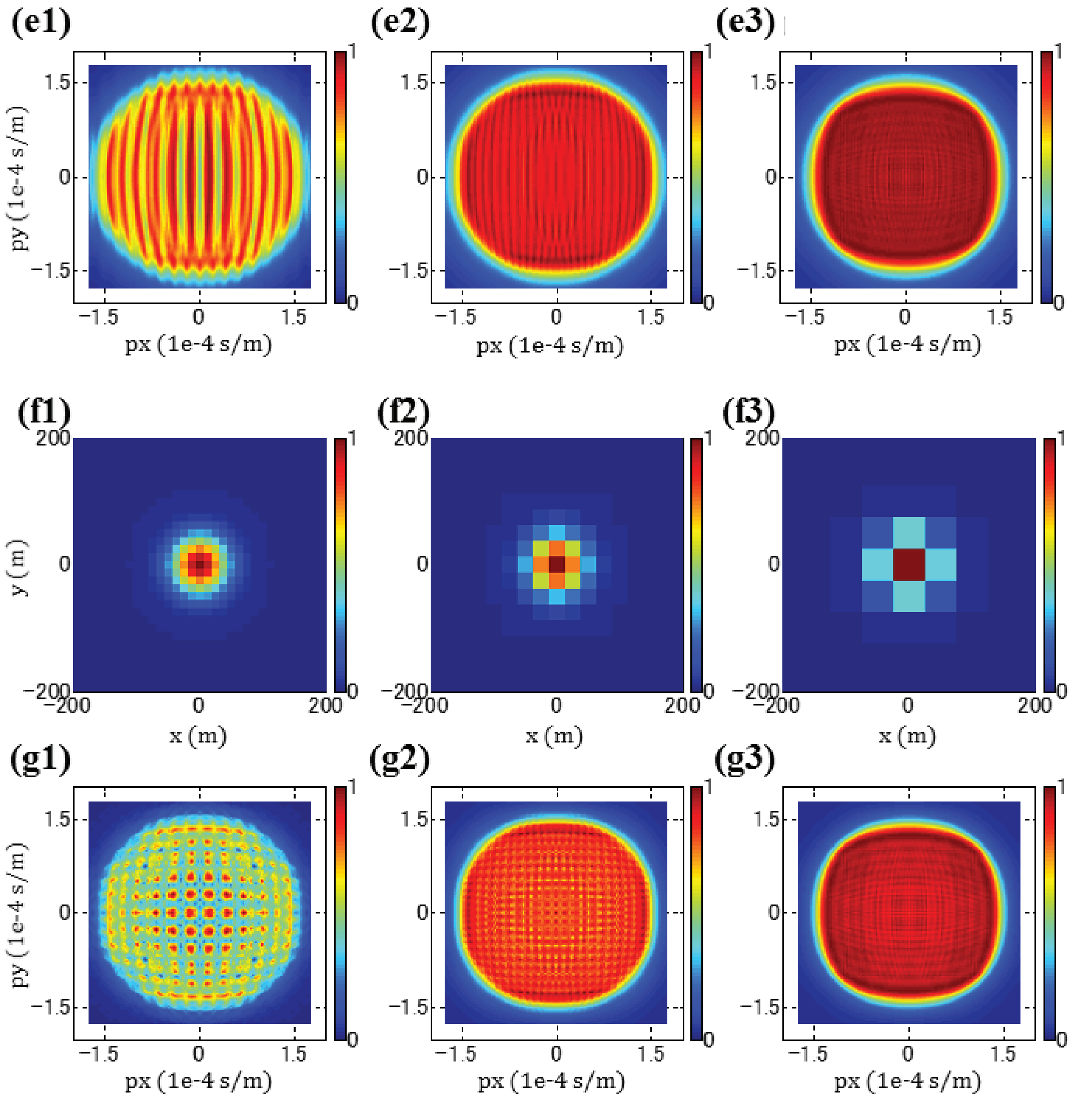

Figure 5. (Continued) (e) the focal source beams in the Radon domain; (f) the zoomed-in images of the resolution functions in the space domain; (g) the AVP functions in the Radon domain. Blue and red in a geometry spread indicate receiver and source locations. Colour scales of focal beams and focal functions represent normalized amplitudes.

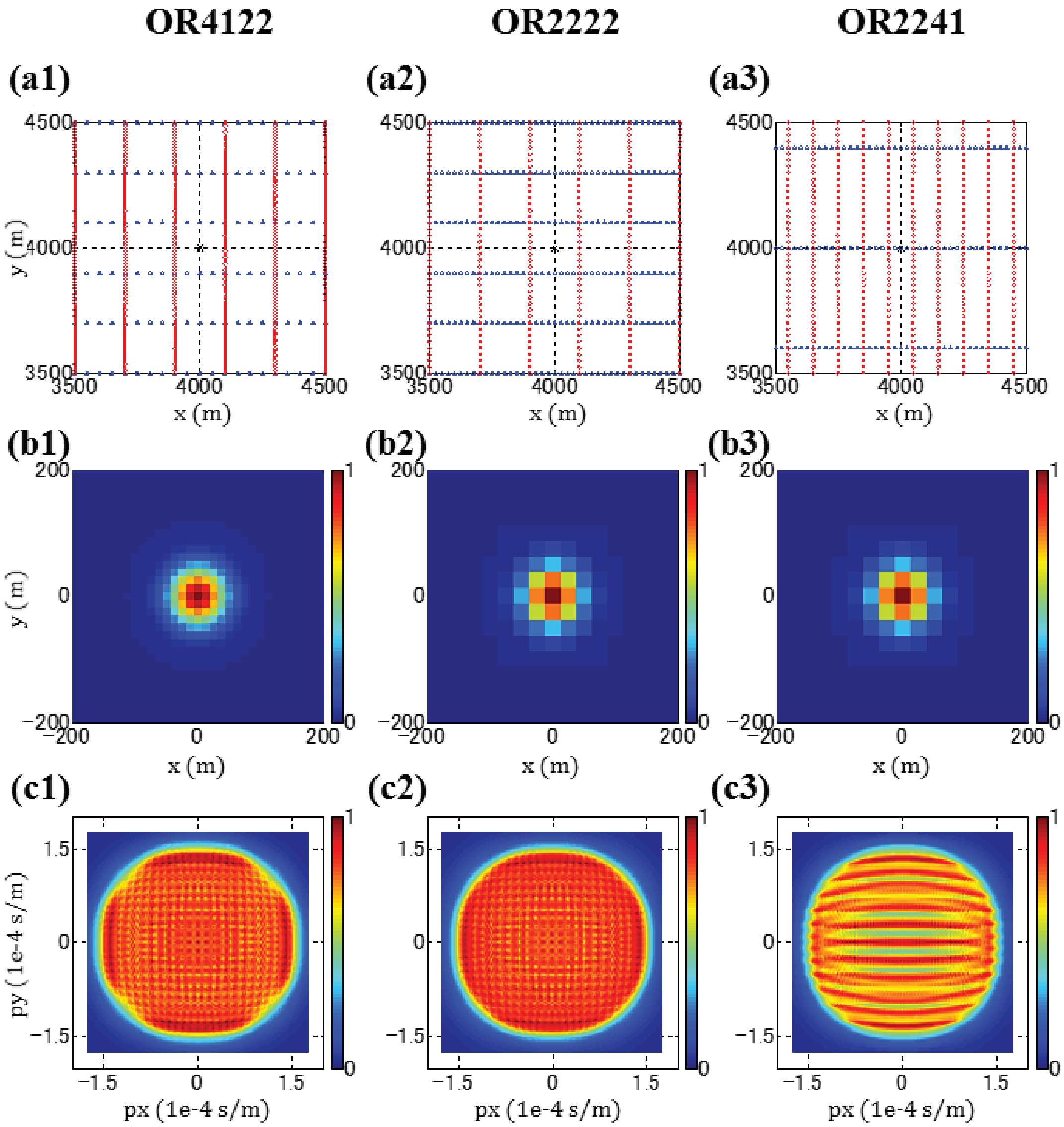

Figure 6. The acquisition geometry spread and focal functions of OR4122 (1^{st} column), OR2222 (2^{nd} column) and OR2241 (3^{rd} column). (a) The geometry spreads around the center; (b) the zoomed-in images of the resolution functions in the space domain; (c) the AVP functions in the Radon domain. (to be continued)

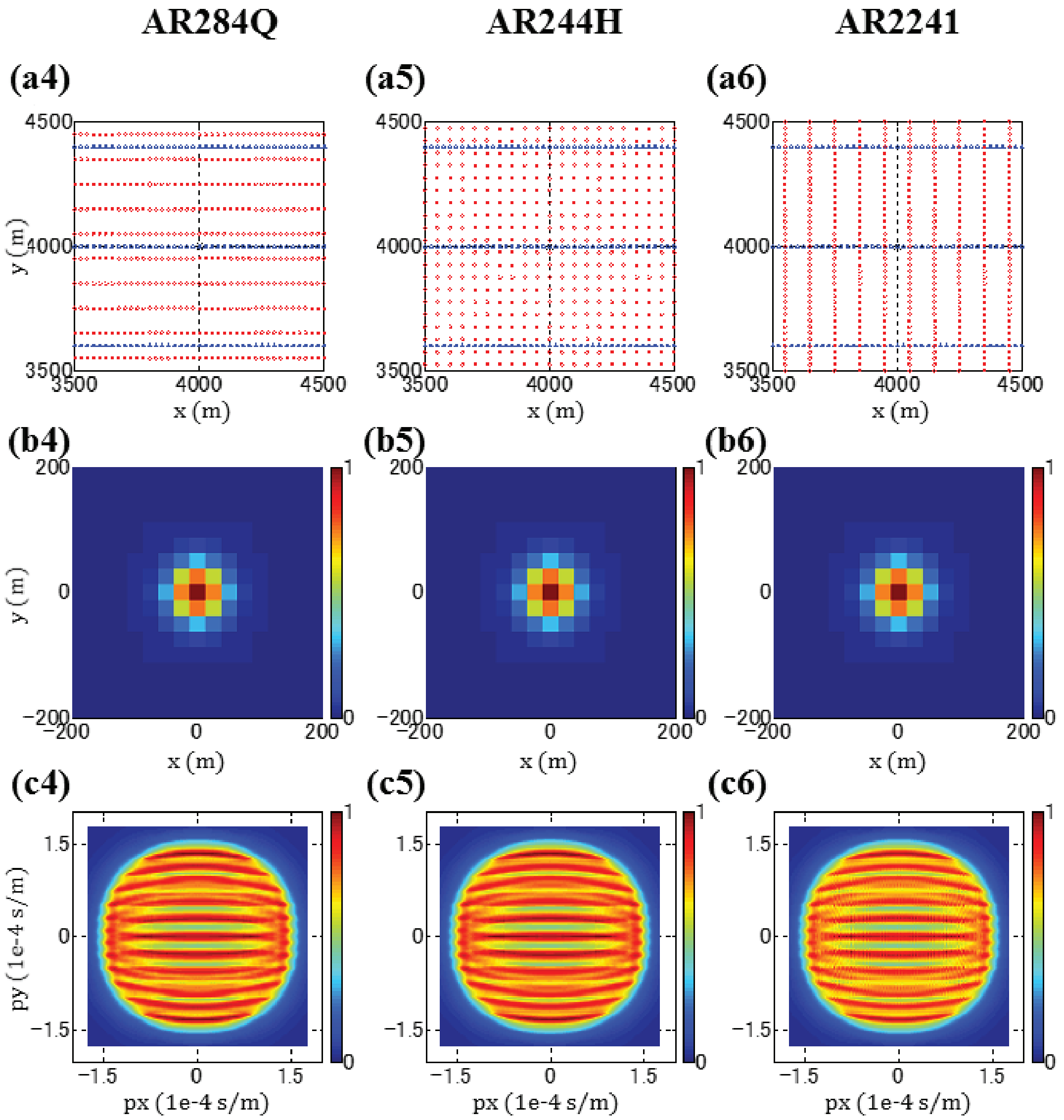

Figure 6. (Continued) The acquisition geometry spread and focal functions of AR284Q (4th column), AR244H (5th column) and AR2241 (6th column). (a) The geometry spreads around the center; (b) the zoomed-in images of the resolution functions in the space domain; (c) the AVP functions in the Radon domain. Blue and red in a geometry spread indicate receiver and source locations. Colour scales of focal beams and focal functions represent normalized amplitudes.

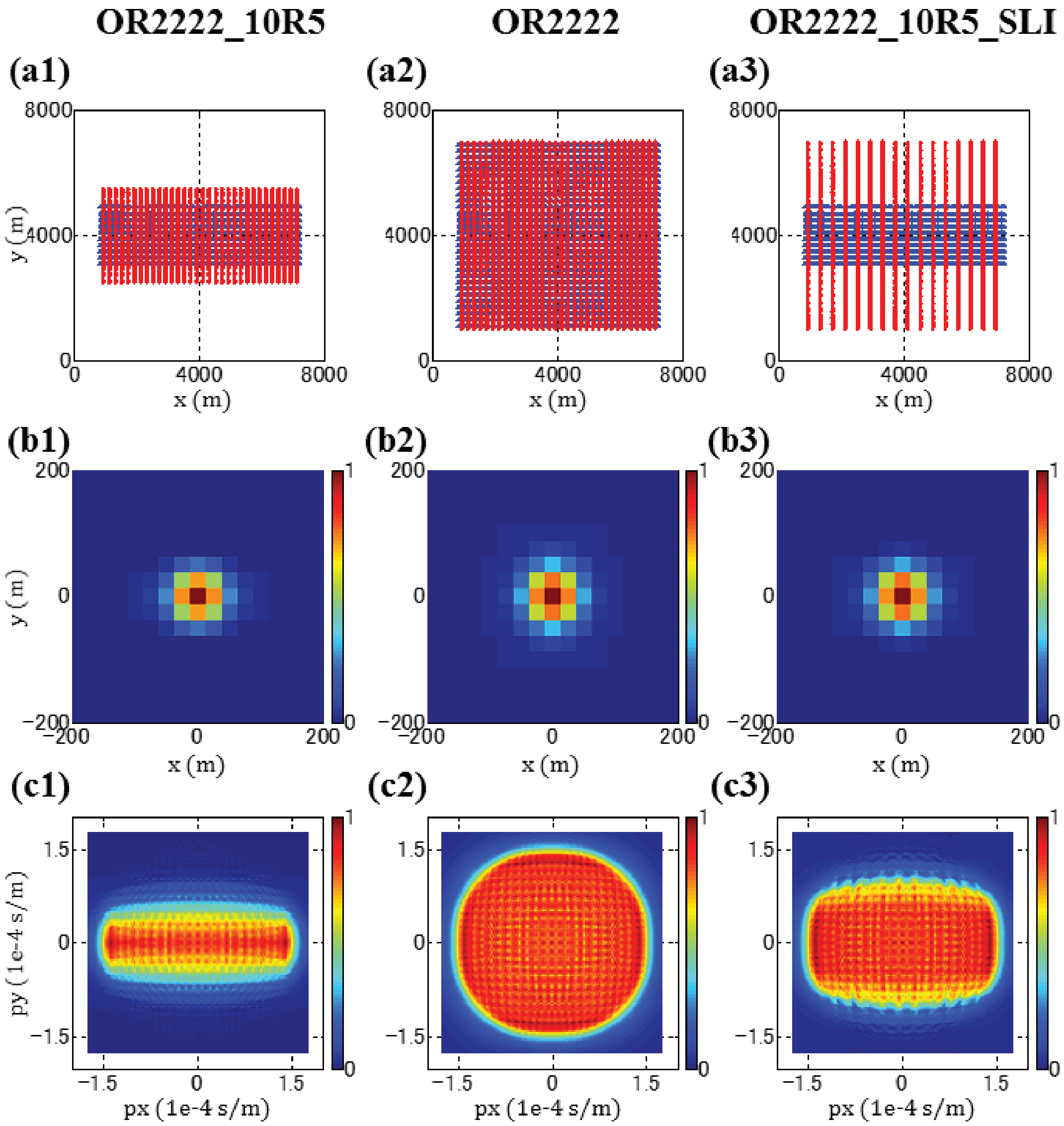

Figure 7. A stationary part of the acquisition geometry and the total focal functions of OR2222_10R5 (1st column), OR2222 (2nd column) and OR2222_10R5_SLI (3rd column). (a) The patch spreads; (b) the zoomed-in images of the resolution functions in the space domain; (c) the AVP functions in the Radon domain. Blue and red in a geometry spread indicate receiver and source locations. Colour scales of focal beams and focal functions represent normalized amplitudes.

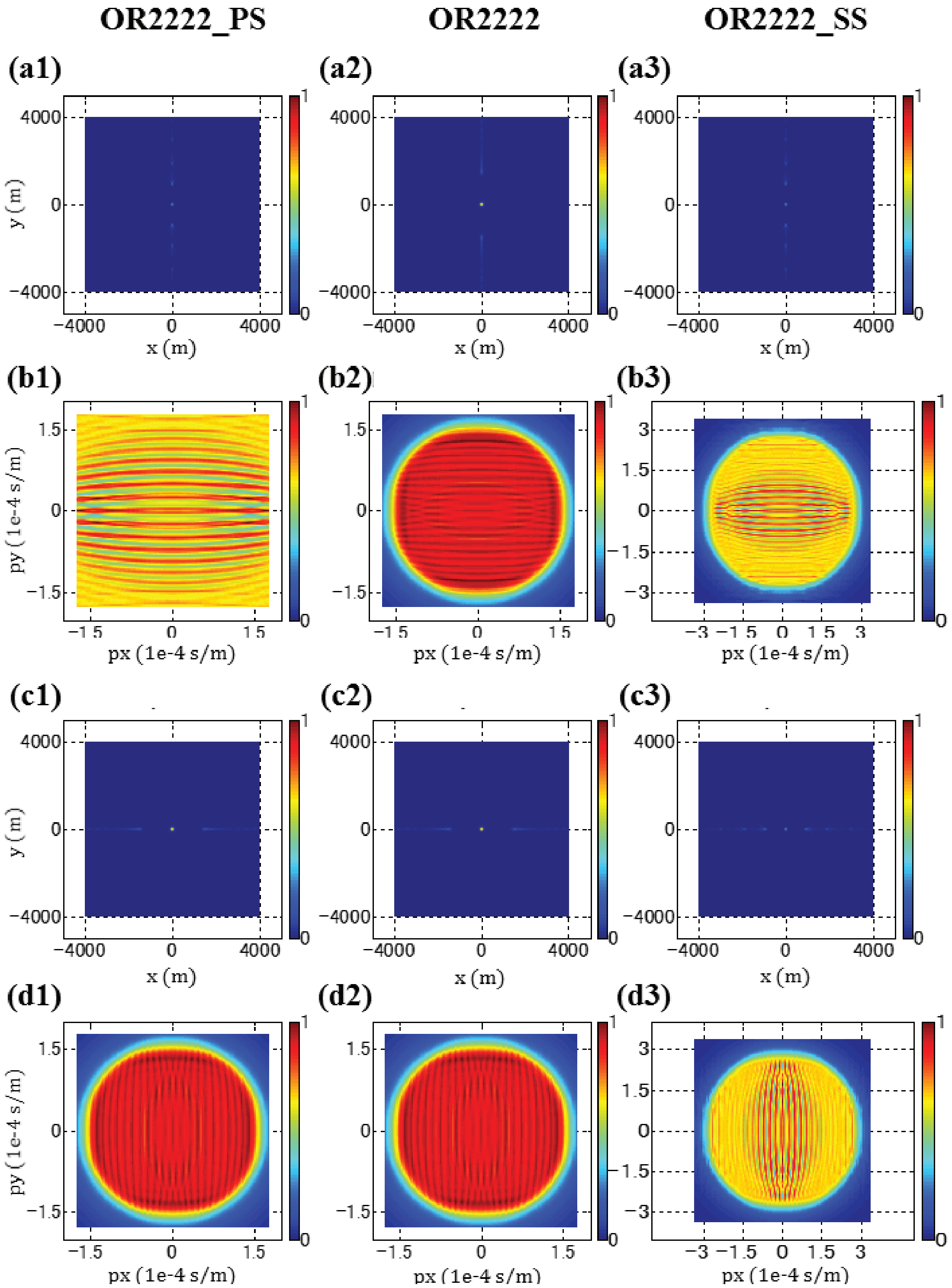

Figure 8. The focal beams and focal functions of OR2222_PS (1st column), OR2222 (2nd column) and OR2222_SS (3rd column). (a) the focal detector beams in the space domain; (b) the focal detector beams in the Radon domain; (c) the focal source beams in the space domain; (d) the focal source beams in the Radon domain; (to be continued)

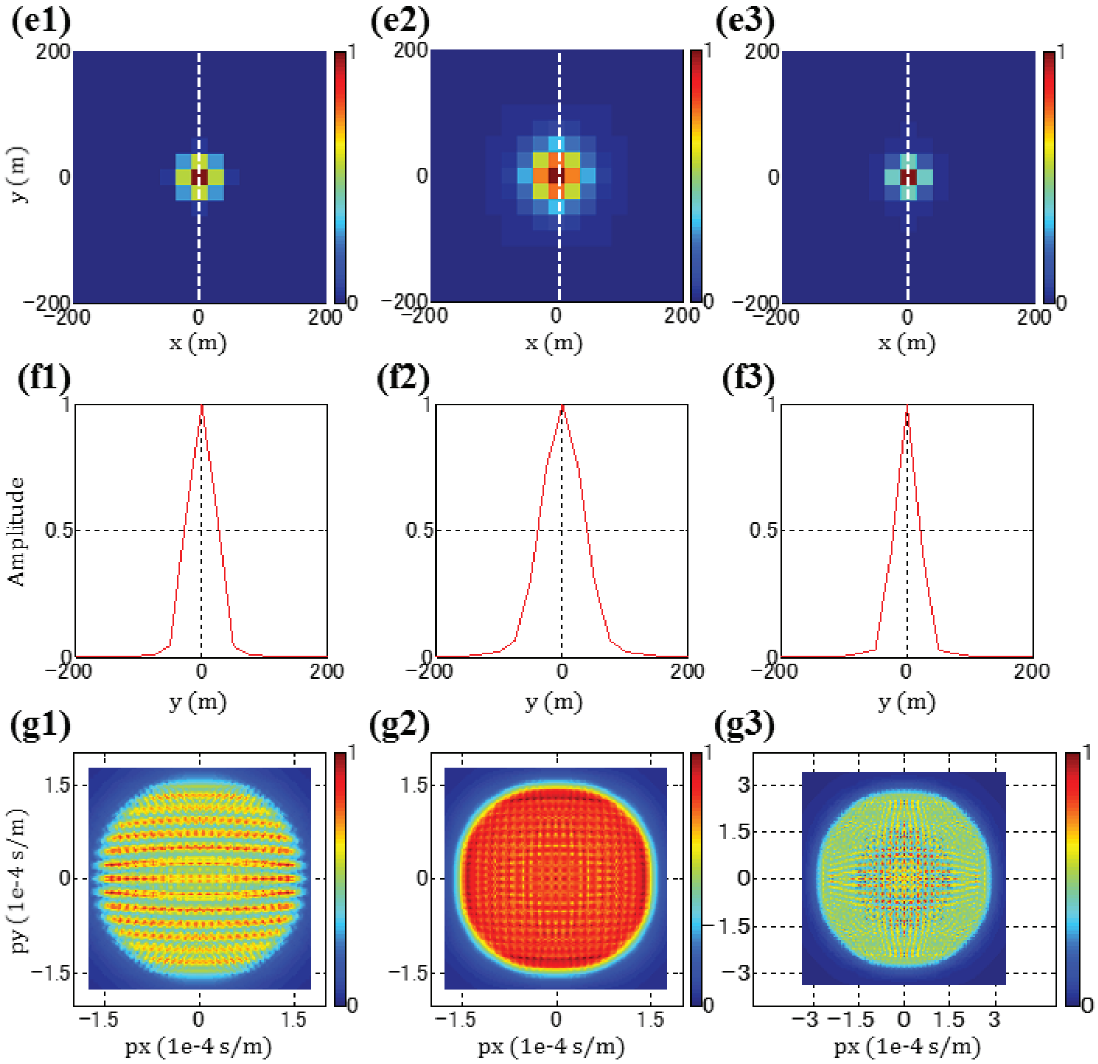

Figure 8. (Continued) (e) the zoomed-in images of the resolution functions in the space domain; (f) the cross sections of the dashed lines on the above; (g) the AVP functions in the Radon domain. Colour scales of focal beams and focal functions represent normalized amplitudes.

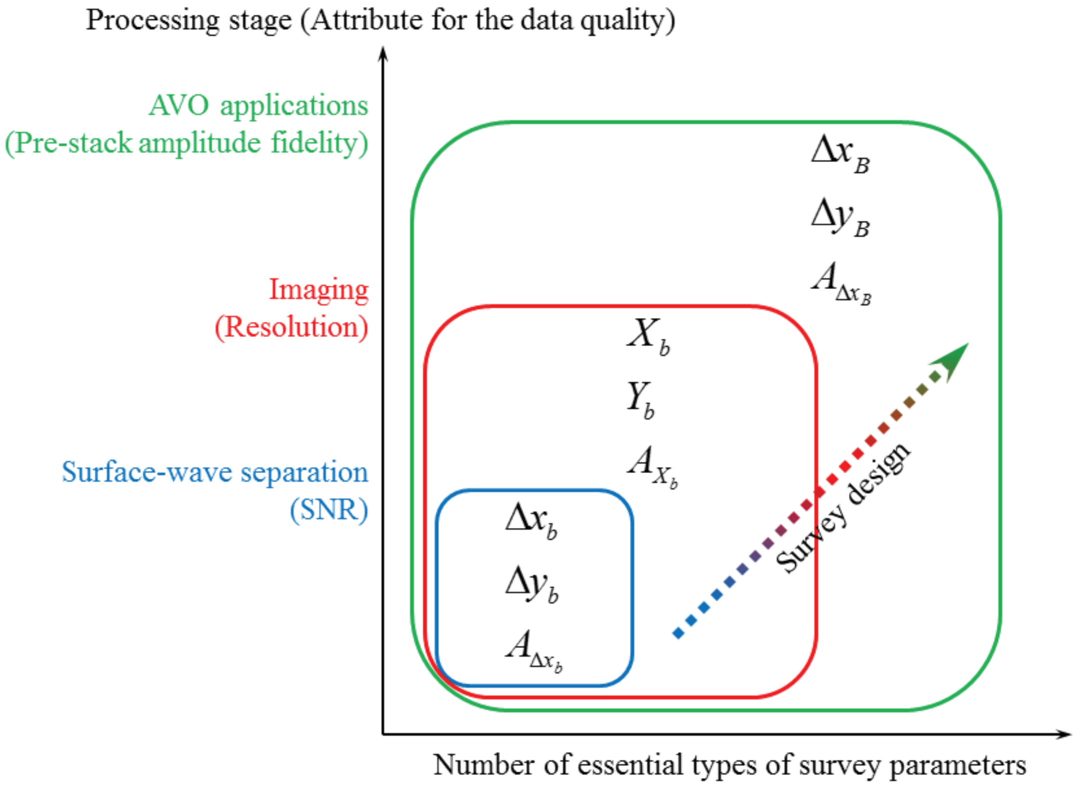

Figure 9. The essential types of survey parameters for surface-wave separation, reflection imaging and AVP applications. Survey parameters should be determined from the lower left to the upper right in the figure.

LIST OF TABLES

Geometry	Δx_d (m)	Δy_s (m)	Δy_d (m)	Δx_s (m)	X_d (m)	Y_s (m)	x_{rep}	y_{rep}	C
OR1144	12.5	12.5	400	400	6400	6000	1	1	1.00
OR2222	25.0	25.0	200	200	6400	6000	1	1	1.00
OR4411	50.0	50.0	100	100	6400	6000	1	1	1.00
OR4122	50.0	12.5	200	200	6400	6000	1	1	1.00
OR2241	25.0	25.0	400	100	6400	6000	1	1	1.00
AR284Q	25.0	100.0	400	25	6400	6000	1	1	1.00
AR244H	25.0	50.0	400	50	6400	6000	1	1	1.00
AR2241	25.0	25.0	400	100	6400	6000	1	1	1.00
OR2222_10R5	25.0	25.0	200	200	6400	3000	1	2	1.00
OR2222_10R5_SLI	25.0	25.0	200	400	6400	6000	1	2	1.00

Geometry	Δx_b (m)	Δy_b (m)	X_b (m)	Y_b (m)	$A_{\Delta x_b}$	A_{X_b}	C_{x_b}	C_{y_b}	C_b
OR1144	12.5	12.5	6400	6000	1.00	0.94	2.00	2.00	4.00
OR2222	25.0	25.0	6400	6000	1.00	0.94	1.00	1.00	1.00
OR4411	50.0	50.0	6400	6000	1.00	0.94	0.50	0.50	0.25
OR4122	50.0	12.5	6400	6000	4.00	0.94	0.50	2.00	1.00
OR2241	25.0	25.0	6400	6000	1.00	0.94	1.00	1.00	1.00
AR284Q	25.0	100.0	6400	6000	0.25	0.94	1.00	0.25	0.25
AR244H	50.0	50.0	6400	6000	1.00	0.94	0.50	0.50	0.25
AR2241	100.0	25.0	6400	6000	4.00	0.94	0.25	1.00	0.25
OR2222_10R5	25.0	25.0	6400	3000	1.00	0.47	1.00	0.50	0.50
OR2222_10R5_SLI	25.0	25.0	6400	6000	1.00	0.94	1.00	1.00	1.00

Geometry	Δx_B (m)	Δy_B (m)	X_B (m)	Y_B (m)	$A_{\Delta x_B}$	A_{X_B}	C_{x_B}	C_{y_B}	C_B
OR1144	400	400	6400	6000	1.00	0.94	0.50	0.50	0.25
OR2222	200	200	6400	6000	1.00	0.94	1.00	1.00	1.00
OR4411	100	100	6400	6000	1.00	0.94	2.00	2.00	4.00
OR4122	200	200	6400	6000	1.00	0.94	1.00	1.00	1.00
OR2241	400	100	6400	6000	4.00	0.94	0.50	2.00	1.00
AR284Q	25	400	6400	6000	0.06	0.94	8.00	0.50	4.00
AR244H	25	400	6400	6000	0.06	0.94	8.00	0.50	4.00
AR2241	25	400	6400	6000	0.06	0.94	8.00	0.50	4.00
OR2222_10R5	200	200	6400	3000	1.00	0.47	1.00	2.00	2.00
OR2222_10R5_SLI	200	400	6400	6000	0.50	0.94	1.00	1.00	1.00

Table 1. List of the template geometries.